nks
Nordisk kernesikkerhedsforskning
Norrænar kjarnöryggisrannsóknir
Pohjoismainen ydinturvallisuustutkimus
Nordisk kjernesikkerhetsforskning
Nordisk kärnsäkerhetsforskning
Nordic nuclear safety research

NKS-209
ISBN 978-87-7893-278-5

Modelling of blowdown of steam in the pressurized PPOOLEX facility

Timo Pättikangas, Jarto Niemi and Antti Timperi

VTT Technical Research Centre of Finland

December 2009

Abstract

PPOOLEX experiment WLL-04-02 on condensation of vapour is studied with CFD simulations. Wall condensation model has been adapted to an Euler-Euler multiphase model of the Fluent CFD code for this purpose. In addition, a simple direct-contact condensation model has also been included in the code.
The main focus of the CFD modelling work was on modelling condensation in the drywell. The amount of condensation found in the CFD calculation was in fair agreement with the experiment. The present simulation was so short that the gas flowing into the wetwell contained significant amount of air. The mole fraction of vapour at the outlet of the vent pipe had the maximum value of about 0.3. Therefore, the non-condensable gas strongly affected the direct-contact condensation in the water pool. Much longer simulations are needed in order to study jugging and condensation oscillations.
FSI calculations of the experiments were performed by using the Star-CD, ABAQUS and MpCCI codes. An approximate method that makes possible numerically stable FSI calculations for the experimental facilities was used. The method is based on linear perturbation method which necessitates small structural deformations. The calculations showed that FSI has to be taken into account for the POOLEX facility which has relatively light structures.
A way for determining the pressure source for the acoustic model from pressure measured at the pool bottom was also examined. Separation of the pressure component due to wall motion from the blowdown load was attempted by conducting a Fourier analysis on the measured displacement signal. The study showed that in practise sufficiently accurate acceleration signal cannot be obtained this way because the transformed signal gets easily out of phase. A measurement system was proposed which could be used for determining the pressure fluctuations.

Key words

Condenstion pool, pressure suppression pool, BWR, CFD, fluid-structure interaction, FSI

NKS-209
ISBN 978-87-7893-278-5

Electronic report, December 2009

NKS Secretariat
NKS-776
P.O. Box 49
DK - 4000 Roskilde, Denmark

Phone +45 4677 4045
Fax +45 4677 4046
www.nks.org
e-mail nks@nks.org

Contents

1 Introduction

Experiments with a scaled-down model of a pressure suppression containment of a BWR are performed with the PPOOLEX facility at the Lappeenranta University of Technology (LUT). The experimental facility consists of pressurized drywell and wetwell compartments. Air or vapour is blown into the drywell compartment and it flows through a vent pipe to the wetwell compartment, where vapour is condensed in a water pool. The main interests in these experiments are in the in the thermal hydraulic phenomena in the drywell and the wetwell, and in the pressure loads on the structures of the containment.

In the present report, the experiments performed are studied with Computational Fluid Dynamics Calculations (CFD) and Finite Element Modelling (FEM). In the CFD calculations, the main focus is in the wall condensation that occurs in the drywell. The beginning of the discharge, where vapour is blown into the drywell, is studied in detail. The CFD models needed for analysing the wall condensation are described and included in the Fluent CFD code.

In Fluid-Structure Interaction (FSI) analysis, the motion of the structures is taken into account when the pressure loads on the structures are calculated. FSI has significance in certain situations of the blowdown event (Giencke, 1981; Björndahl and Andersson, 1998). Pressure loads occurring during blowdown have a large range of frequency components and they exert a continuous excitation on the walls. Using only one-way pressure mapping is not necessarily conservative in this kind of situation because the water lowers eigenfrequencies of the structure. In this work, FSI calculations of the POOLEX and PPOOLEX experiments are performed by using Star-CD 4.08 for CFD and ABAQUS 6.7 for structural analysis. The external MpCCI 3.0.6 software is used for coupling the CFD and structural analysis codes. Two-way coupled FSI calculations of the experiments have been numerically unstable with explicit coupling scheme of MpCCI. A linear perturbation method (Huber et al., 1979; Sonin, 1980; Timperi et al., 2007) is therefore used for preventing the numerical instability. The method is validated also against numerical data in blowdown situations.

The pressure source is needed at the blowdown pipe outlet when simplified methods, such as the incompressible potential flow or acoustic models, are used for estimating the pressure loads on the pool walls (Björndahl and Andersson, 1998; Pättikangas et al., 2008). One possibility for determining the pressure source is measuring pressure signal on the pool wall and calculating with the applied model the corresponding source. A major problem with this approach is that the resulting wall motion also affects the pressure signal. This effect has been significant in the POOLEX and PPOOLEX experiments; the pressure loads have been masked by the pressure fluctuations caused by the wall motion. Separation of these two pressure components is attempted in this work by conducting a Fourier analysis on the measured wall displacement signal. Simplified analytical and numerical models of the pool are also used for studying which parameters of the pool affect the pressure fluctuations most.

In the following, CFD modelling of condensation in the experiments with vapour is first discussed. The end part of the report is focussed on the modelling of the fluid-structure interactions. In section 2, the experimental PPOOLEX facility is described. In section 3, CFD model for wall condensation in the drywell is described in detail. Section 4 contains results of CFD modelling of an experiment performed with vapour with the PPOOLEX facility. In section 5, fluid-structure interaction calculations with the POOLEX and PPOOLEX facilities are presented. Section 6 discusses determination of the pressure source for the calculations of the loads on the structures with methods alternative to full CFD calculations. Finally, conclusions are presented in section 7.

2 Experimental setup

In the beginning of year 2009, a series of experiments with vapour were performed at the Lappeenranta University of Technology with the pressurized PPOOLEX test facility. PPOOLEX is designed to model the pressure suppression pool of a Boiling Water Reactor (BWR) with drywell and wetwell compartments. The total height of the PPOOLEX drywell and wetwell compartments is 7.45 meters and the diameter is 2.39 meters. The PPOOLEX facility is shown in figure 1.

The water level in the beginning of the experiments was 2.14 m from the bottom of the pool. The submergence of the DN200 vent pipe was 1.05 m, which corresponds to a hydrostatic pressure of about 10.2 kPa at the vent pipe outlet.

In the experiments, pure vapour was blown into the drywell compartment of the PPOOLEX facility through the horizontal DN200 pipe. Vapour was obtained from the PACTEL steam generator connected to the DN200 pipe with a DN50 pipe. The mass flow rate of vapour into the drywell was measured with a vortex meter located in the DN50 line. In addition, the temperature of vapour was measured in the inlet plenum. The measured mass flow rate and temperature were used as boundary conditions in the CFD simulations.

Three different condensation phenomena occur in the experiments. First, some bulk condensation of vapour may occur, when vapour flows from the DN50 pipe through the DN200 inlet plenum into the dry well. Second, part of the vapour is condensed on the walls of the drywell. The wall condensation is determined by the initial wall temperature in the drywell and by the heat transfer through the walls of the drywell to the laboratory. Third, direct-contact condensation occurs in the water pool of the wetwell, when vapour flows from the drywell to the wetwell. In the early part of the experiment, the gas flowing to the wetwell contains mainly non-condensable air and only small fraction of vapour. In later phases of the discharge, almost pure vapour flows to the wetwell.

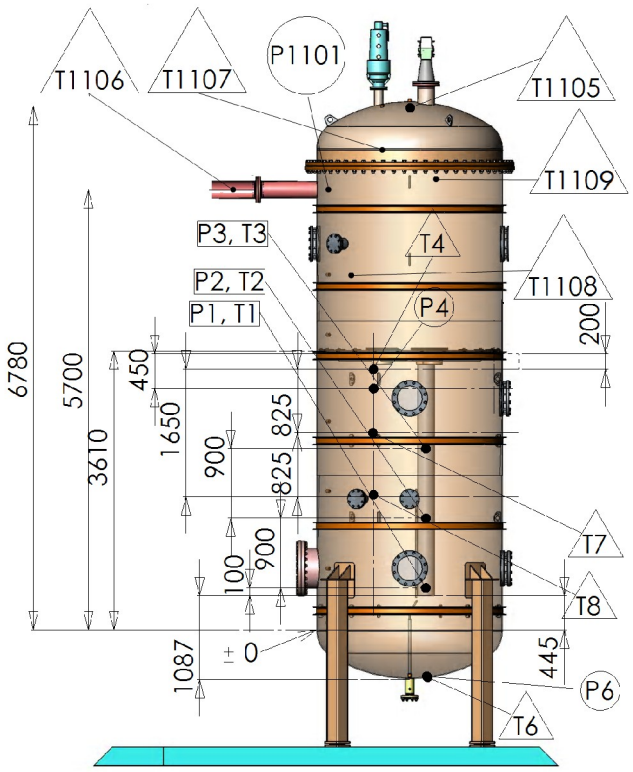

Figure 1. Pressure (Pn) and temperature (Tn) measurements in the PPOOLEX pressurized test facility at Lappeenranta University of Technology (Laine and Puustinen, 2008).

In the following sections, early phase of a vapour discharge is modelled by using Euler-Euler two-phase model for vapour, air and water. In the Euler-Euler model, the conservation equations of mass, momentum and energy are solved for both the gas and liquid phases. The gas phase is assumed to consist of two species: air and vapour. The flow equations are solved with the commercial Fluent 6.3.26 CFD code, where the relevant condensation models have been implemented as User-Defined Functions.

3 CFD model for condensation

The following model is intended to describe basic features of wall condensation for two-phase fluid simulations with the Fluent CFD code. Heat is transferred from the gas phase through a liquid film to the solid wall. The heat and mass transfer between the gas phase, film and the solid wall is illustrated in figure 2.

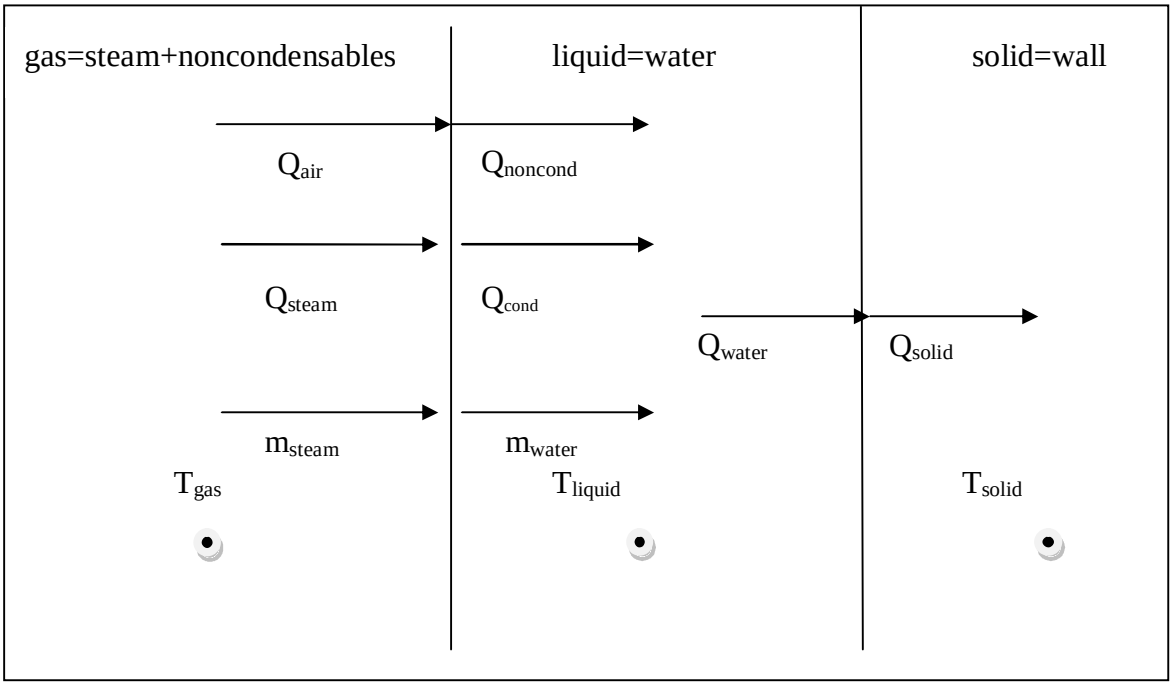

Figure 2. Heat transfer from the gas phase through the liquid film to the solid wall.

The wall condensation model is applied in the grid cell adjacent to the wall in the numerical CFD mesh. When the mass and heat transfer are modelled, the following properties of the gas phase, liquid film and solid wall are used:

- gas temperature (T_{gas}), mole fraction of vapour (Y_{steam})
- liquid temperature (T_{liquid}), solid temperature (T_{solid})
- heat and mass transfer coefficients (htc_{gas}, htc_{liquid}, htc_{solid}, mtc_{steam})

The gas phase is treated as a two-component mixture with a condensable and a non-condensable gas component. The effects of the mixture components to the heat transfer are estimated by using the volume fractions of the components. That is, the heat transfer area is reduced by the mole fraction of the component.

If liquid water exists in the grid cell adjacent to the wall, it is assumed that water forms a film on the wall as is depicted in figure 2. Therefore, the wall mass and heat transfer is always a single-phase phenomenon: gas-solid or liquid-solid interaction. The mass and heat transfer at the fluid-solid interface is determined by the properties of the fluid phase (T_{gas} or T_{liquid}) and the properties of the solid (T_{solid}). Mass and heat transfer at the gas-liquid interface is determined by the phase properties of the fluids (T_{gas}, T_{liquid}).

3.1 Gas-solid interface

When there is no water in the grid cell adjacent to the wall, evaporation of liquid is not possible. Then, the heat transfer process of the non-condensable gas component is:

$$Q_{air} = Q_{noncond} = w_{air} \frac{htc_{gas} \cdot htc_{solid}}{htc_{gas} + htc_{solid}} \left(T_{gas} - T_{solid}\right) \quad (1)$$

Here, w_{air} stands for the mole fraction of air.

Heat transfer process of the condensable gas component is modelled in the following way. The condensation state is determined by comparing the interface temperature T_i to steam saturation temperature T_{sat}:

$$T_i = \frac{htc_{gas} \cdot T_{gas} + htc_{solid} \cdot T_{solid}}{htc_{gas} + htc_{solid}} \quad (2)$$

If $T_i \geq T_{sat}(p_{steam})$, then no condensation is possible and the steam heat flux is

$$Q_{steam} = Q_{cond} = w_{steam} \frac{htc_{gas} \cdot htc_{solid}}{htc_{gas} + htc_{solid}} \left(T_{gas} - T_{solid}\right) \quad (3)$$

If $T_i < T_{sat}(p_{steam})$, condensation takes place at the saturation temperature:

$$\begin{aligned} Q_{steam} &= w_{steam} \cdot htc_{gas} \left(T_{gas} - T_{sat}\right) \\ Q_{cond} &= w_{steam} \cdot htc_{solid} \left(T_{sat} - T_{solid}\right) \end{aligned} \quad (4)$$

The condensation mass flux is determined by the energy balance at the interface:

$$\dot{m}''_{steam} = \frac{Q_{cond} - Q_{steam}}{h_{fg} + C_{p,gas}\left(T_{gas} - T_{sat}\right)} \quad (5)$$

The total gas heat flux is

$$Q_{gas} = Q_{air} + Q_{steam} \quad (6)$$

and the total solid heat flux is

$$Q_{solid} = Q_{cond} + Q_{noncond} \quad (7)$$

3.2 Gas-liquid interface

When the grid cell adjacent to the wall contains liquid water, the heat transfer on the gas-liquid interface has also to be considered. The heat transfer of the non-condensable gas component is determined by

$$Q_{air} = Q_{noncond} = w_{air} \frac{htc_{gas} \cdot htc_{liquid}}{htc_{gas} + htc_{liquid}} \left(T_{gas} - T_{liquid}\right) \quad (8)$$

The condensation/evaporation is determined by the saturation temperature of the condensable gas component:

$$T_{sat} = T_{sat}(p_{steam}) \quad (9)$$

$$Q_{steam} = w_{steam} \cdot htc_{gas} \left(T_{gas} - T_{sat}\right) \quad (10)$$

$$Q_{cond} = w_{steam} \cdot htc_{liquid} \left(T_{sat} - T_{liquid}\right) \quad (11)$$

In the condensation case, i.e., when $Q_{cond} > Q_{steam}$, the steam mass flux is determined by

$$\dot{m}''_{steam} = \frac{Q_{cond} - Q_{steam}}{h_{fg} + C_{p,gas}\left(T_{gas} - T_{sat}\right)} \tag{12}$$

In the evaporation case, the mass flux of steam is determined by

$$\dot{m}''_{steam} = \frac{Q_{cond} - Q_{steam}}{h_{fg} - C_{p,liquid}\left(T_{liquid} - T_{sat}\right)} \tag{13}$$

The heat flow at the liquid-solid interface is

$$Q_{water} = \frac{htc_{liquid} \cdot htc_{solid}}{htc_{liquid} + htc_{solid}}\left(T_{liquid} - T_{solid}\right) \tag{14}$$

The total gas heat flux is

$$Q_{gas} = Q_{air} + Q_{steam} \tag{15}$$

The net heat flux of the liquid is

$$Q_{liquid} = Q_{cond} + Q_{noncond} - Q_{water} \tag{16}$$

and the solid heat flux is

$$Q_{solid} = Q_{water} \tag{17}$$

We finally present a remark on the treatment of the multiple components in the gas phase in the above formulas. If the gas phase consists of many components, the gas components occupy the same volume and share the same heat transfer area. The effective heat transfer area for each gas component can be estimated by reducing the area with the volume fraction of the component. The effect of the reduction can be defined directly for the heat flux Q_{12}:

$$\begin{aligned} &Q'_{12} = w \cdot Q_{12} \\ &\Rightarrow \\ &Q'_{12} = \frac{w \cdot htc_1 \cdot w \cdot htc_2}{w \cdot htc_1 + w \cdot htc_2}\left(T_1 - T_2\right) \end{aligned} \tag{18}$$

where we have $T'_i = T_i$. Equation (18) can now be rewritten as

$$Q'_{12} = \frac{htc'_1 \cdot htc'_2}{htc'_1 + htc'_2}\left(T_1 - T_2\right) \tag{19}$$

$$\begin{aligned} htc'_1 &= w \cdot htc_1 \\ htc'_2 &= w \cdot htc_2 \end{aligned}$$

3.3 Direct-contact condensation

In modeling direct-contact condensation in the wetwell, a simple formulation presented earlier is used (Timperi et al., 2007). The model has now been adapted to the Euler-Euler multiphase model from the Volume Of Fluid (VOF) model that was used in our earlier work. The main focus in the present simulation was in testing the model for wall-condensation.

4 CFD modeling of steam experiments

4.1 CFD model for the wall condensation experiments

The CFD simulations were performed by using the Euler-Euler model of the Fluent 6.3.26 CFD code. The numerical CFD mesh consisted of 135 000 hexahedral grid cells. The mesh was the same as in our earlier simulations of air discharges with PPOOLEX experimental facility (see Pättikangas et al., 2008).

The early phase of the PPOOLEX experiment WLL-05-02 was chosen to be modeled. In this experiment, the wall of the drywell was preheated with steam in order to reduce the amount of wall condensation and to enhance the amount of vapour flowing into the wetwell. The initial wall temperature was about 60 °C. After preheating, the drywell was opened and air flowed into the drywell. In the modeling, it was assumed that the drywell initially contained mixture of air and saturated vapour.

The mass flow rate of vapour into the drywell in the experiment is shown in figure 3. The maximum flow rate was about 550 g/s. The measurement indicated that the maximum flow rate was achieved at time t = 4.5 s. The vortex meter may have some delay in the starting phase of the discharge. The measured mass flow rate was, however, used as the boundary value without assuming any delays in the mass flow rate measurement.

In the experiment, the temperature of the vapour was measured in the DN50 line a few meters from the DN200 inlet plenum, where the inlet boundary condition for the CFD calculation is defined. In the CFD calculations, saturated temperature of T = 160 °C was used as the boundary for the temperature of the vapour in the inlet plenum. The temperature measurement of the inlet plenum could not be used as boundary condition because in the early phase of the experiment it is affected by the air in the inlet plenum.

In figure 3, the calculated mass flow rate of air and vapour through the vent pipe from the drywell to the wetwell is shown. The vent pipe is cleared at time t = 6 s and the first bubble is formed at the outlet of the vent pipe in the water pool. After this, new bubbles are formed with a period of about 0.7 s. The period is somewhat shorter than in the air discharges modeled earlier by using the VOF model. In the air discharges the period was found to be about 0.9 s, but it depended on the mass flow rate of the discharge.

In the simulation, some changes were made in the heat transfer modeling between the gas and liquid phase of the Euler-Euler model. Initially, the Ranz-Marshall model readily available in Fluent was used for the heat transfer between the phases. At time t = 12 s, the heat transfer between the phases was turned off in the grid cells that were not adjacent to the wall. This can be seen in figure 3 as an increase in the bubble size after time t = 12 s. Some more testing for finding a better modeling method for the heat transfer between the phases is still needed.

In figure 4, the formation of the first bubble in the wetwell is shown. Since the drywell contains initially mainly air, the first bubbles consist of almost pure air with only a small amount of vapour in the mixture. Therefore, in the early phase

of the dischange, direct-contact condensation in the wetwell is not very significant. The vent pipe is cleared at t = 4 s and the first bubble is formed time t = 5 s. The first bubble reaches the water surface in the wetwell at time t = 5.4 s.

When the present Euler-Euler simulation results are compared with our earlier results obtained with the VOF model, it is found that with Euler-Euler model the interface between the phases is much more diffuse than with the VOF model. This can in particular be seen in the vent pipe in the early phase of the discharge (see figure 4). The difference is due to the modeling techniques used in the VOF method, where the interface between the phases is tracked and numerically kept sharp. In the Euler-Euler method, numerical diffusion has a bigger effect on the interface between the phases.

In figure 5, the bubbles are shown by plotting the isosurfaces of the void fraction at the outlet of the vent pipe. The isosurface $\alpha = 0.05$ is coloured with the vertical velocity of vapour. First, a nice but small bubble is formed at the outlet of the vent pipe. Then, it transforms into a plume of bubbles rising upwards near the vent pipe.

In figure 6, the temperature of the gas phase is shown during the early phase of the discharge. The hot vapour jet can be seen to bend somewhat downwards when it propagates through the drywell and hits the wall opposite to the inlet plenum. At time t = 15 s, the temperature of the drywell varies between 80 and 160 °C.

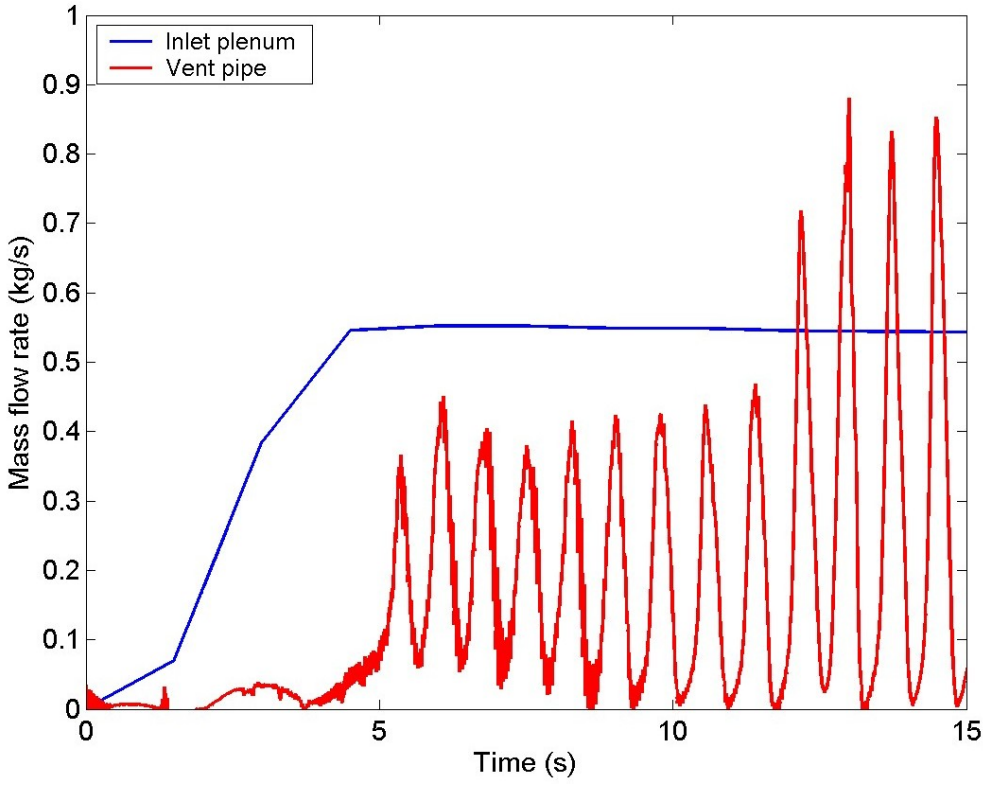

Figure 3. Mass flow rate (kg/s) into the drywell (blue line) and through the vent pipe (red line) versus time (s). Simulation of experiment WLL-05-02.

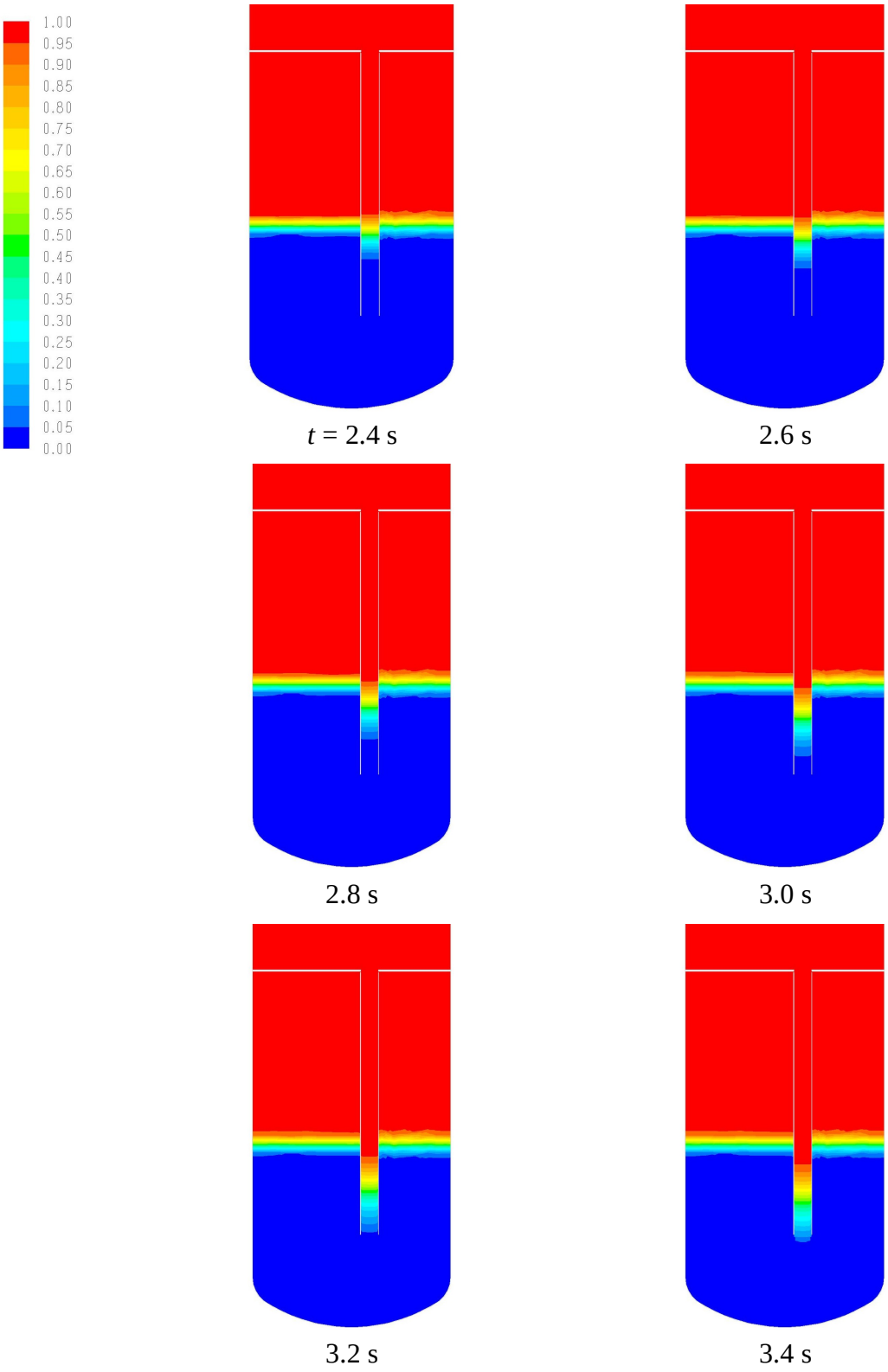

Figure 4. Volume fraction of gas in the vent cross-section of the test facility. Simulation of experiment WLL-05-02 (continues on the following pages).

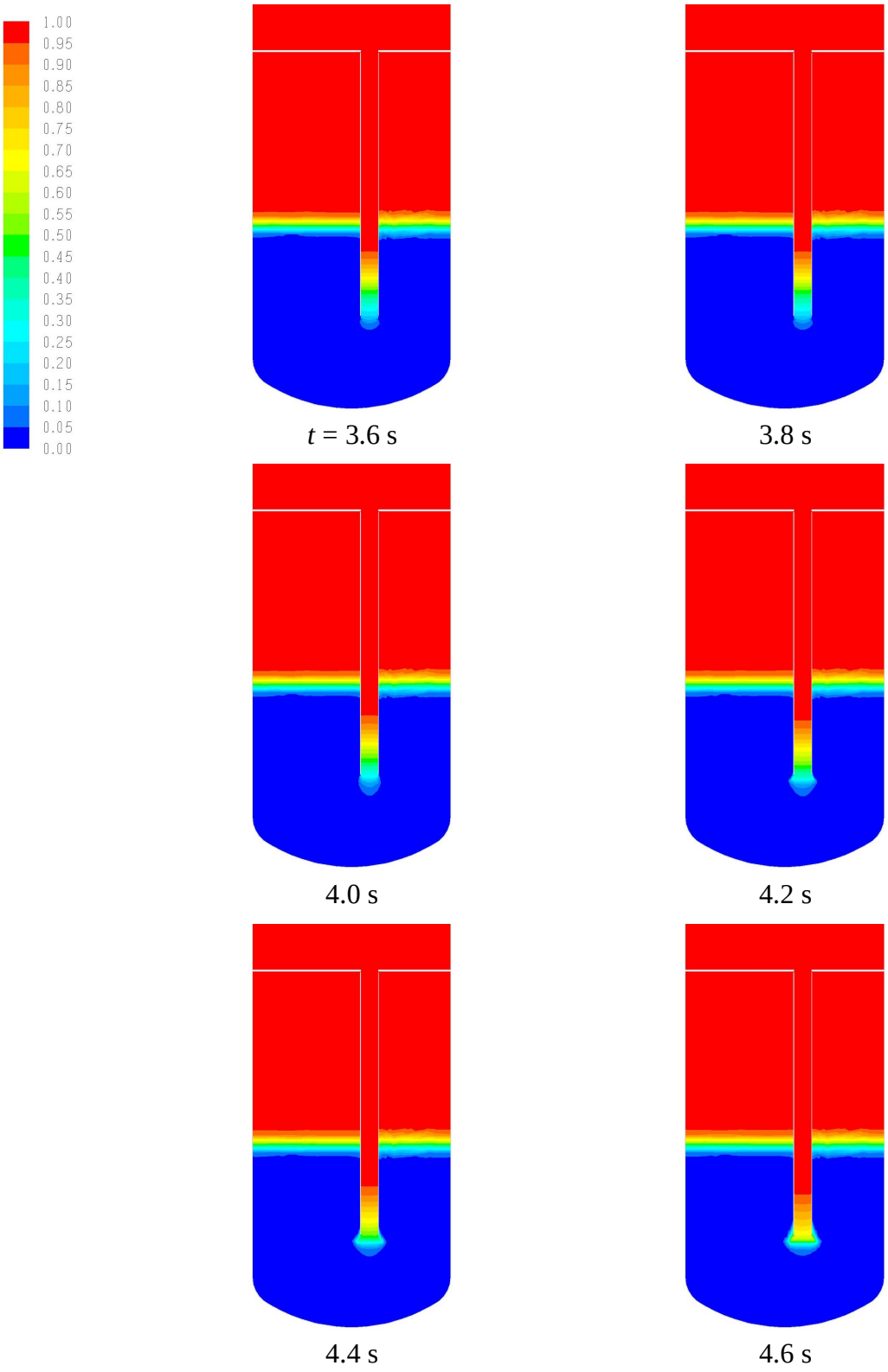

Figure 4. Continues from the previous page.

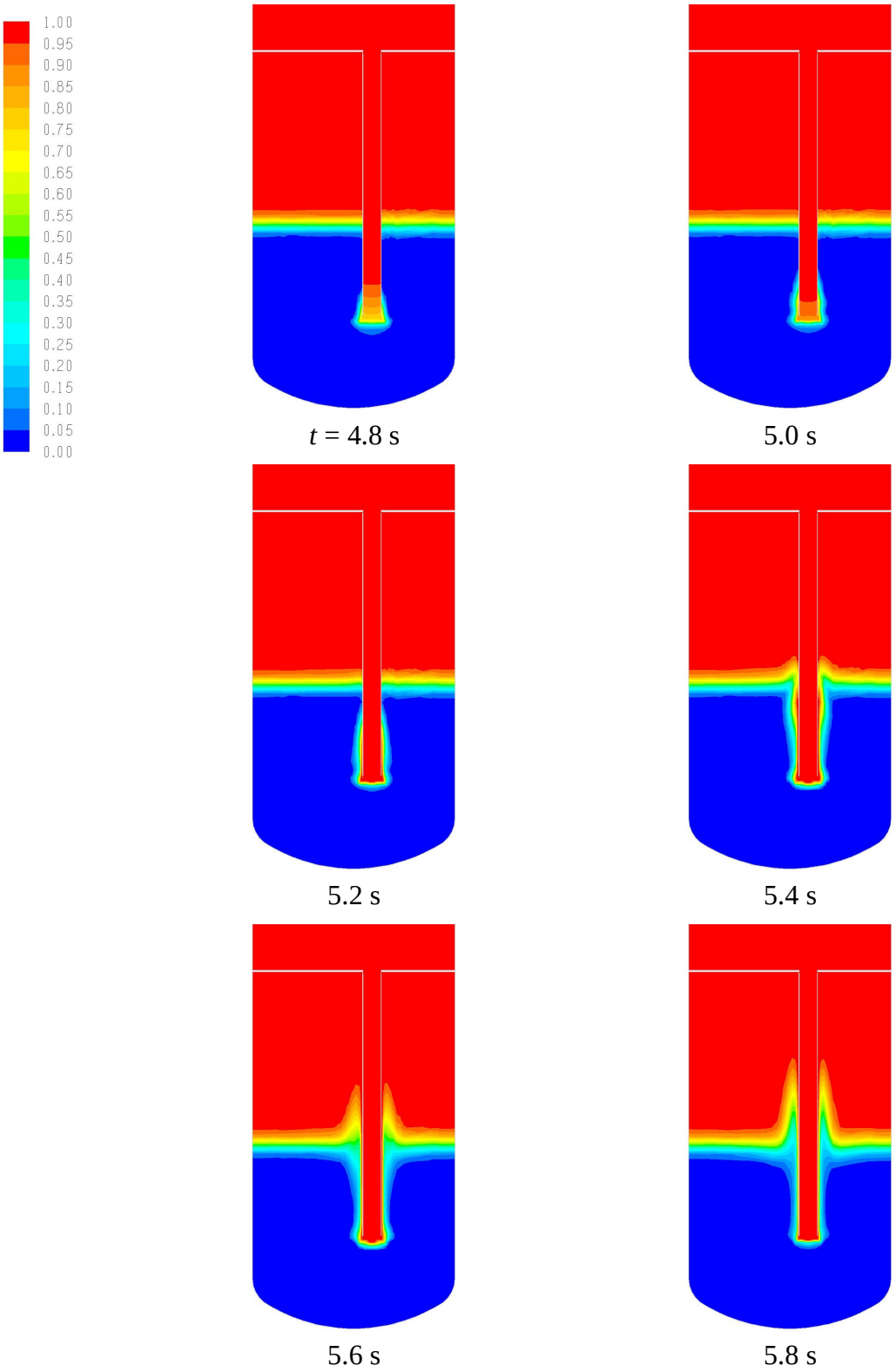

Figure 4. Continues from the previous pages.

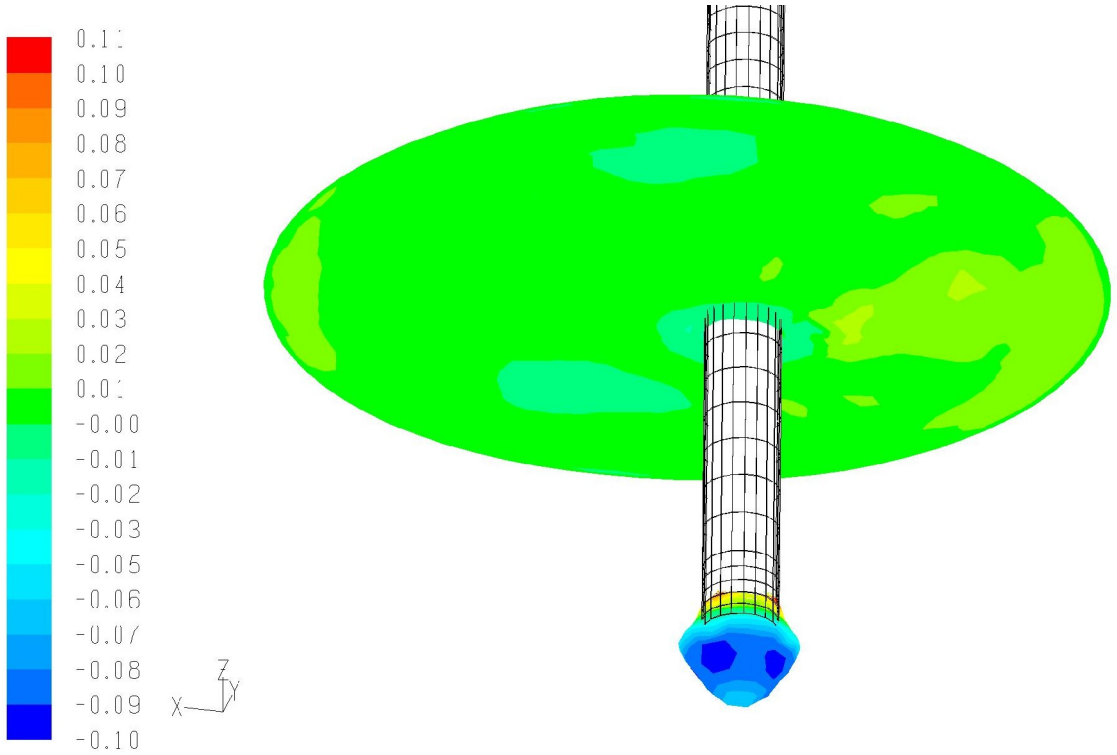

t = 4.2 s

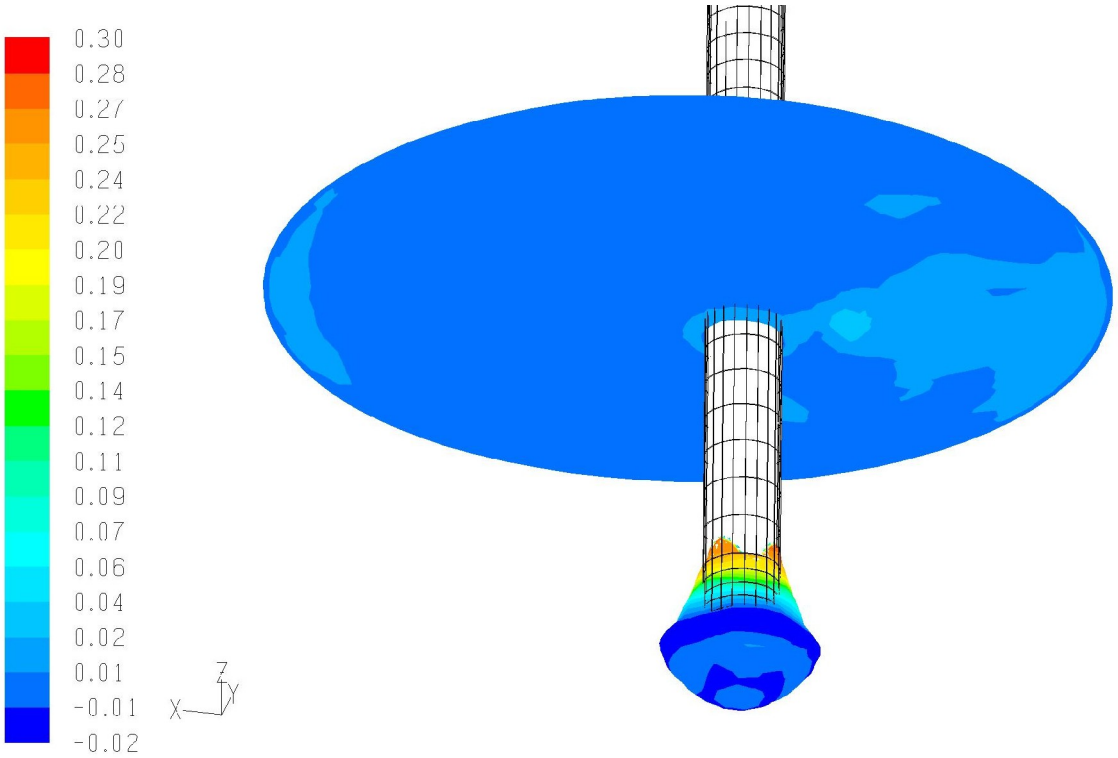

4.6 s

Figure 5. Surface of the bubble coloured with vertical velocity of vapour (m/s). Simulation of experiment WLL-05-02 (continues on the following page).

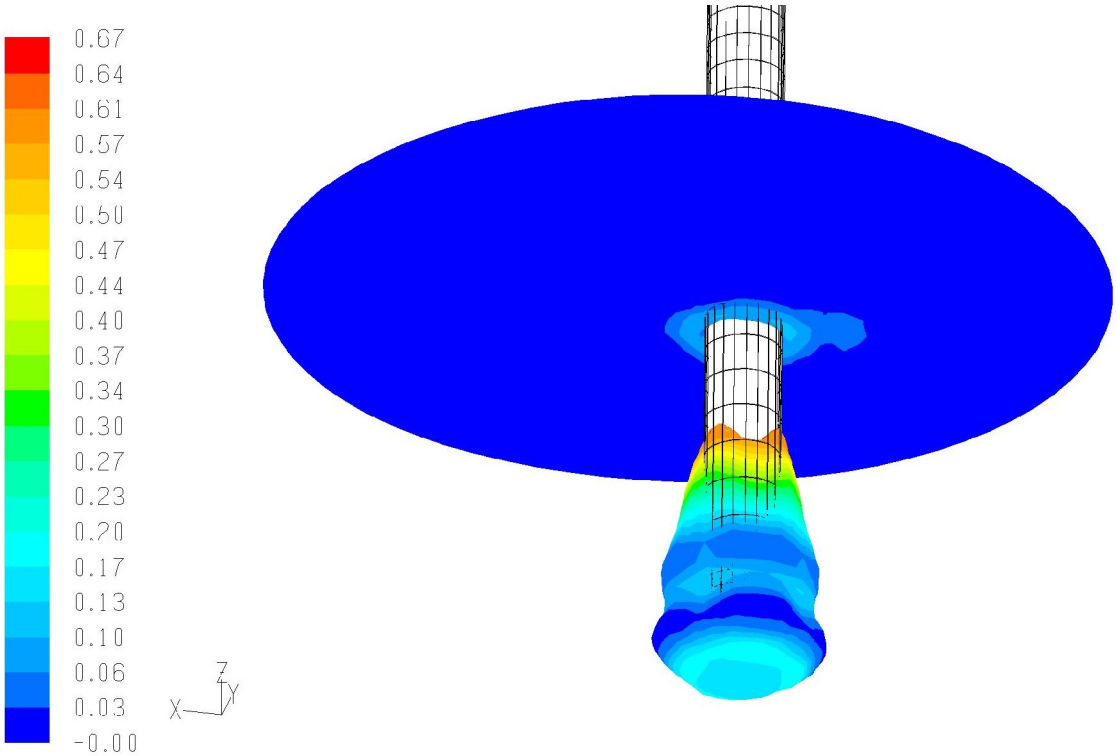

t = 5.0 s

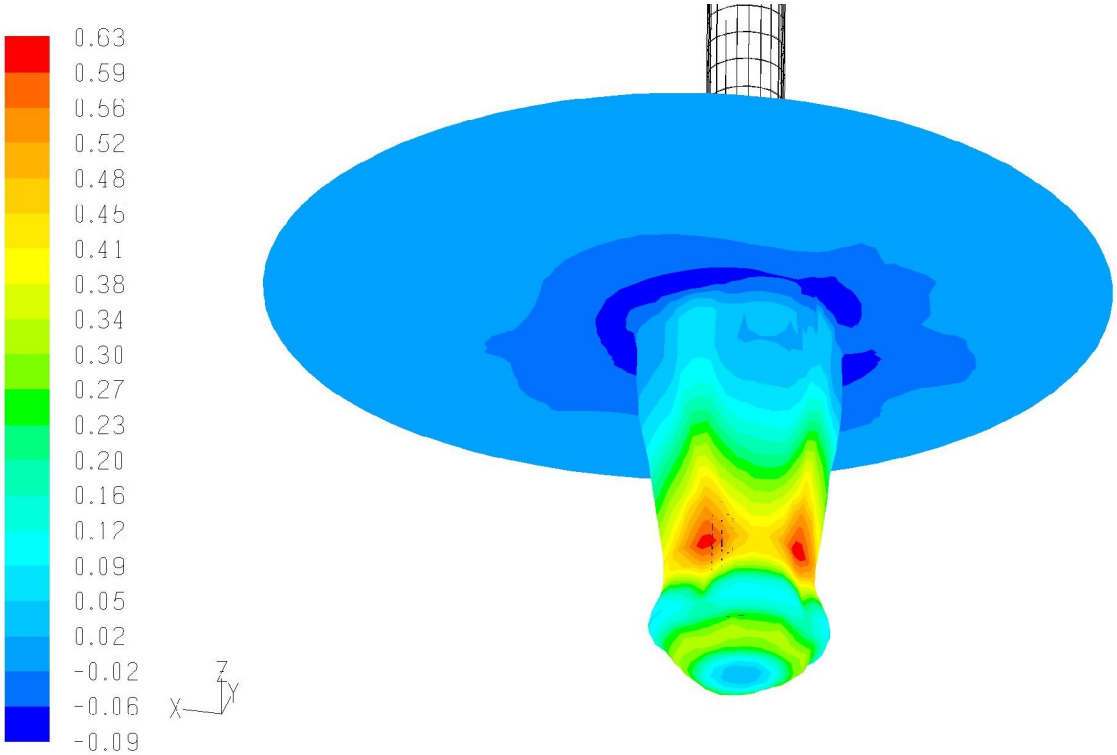

5.4 s

Figure 5. Continues from the previous page.

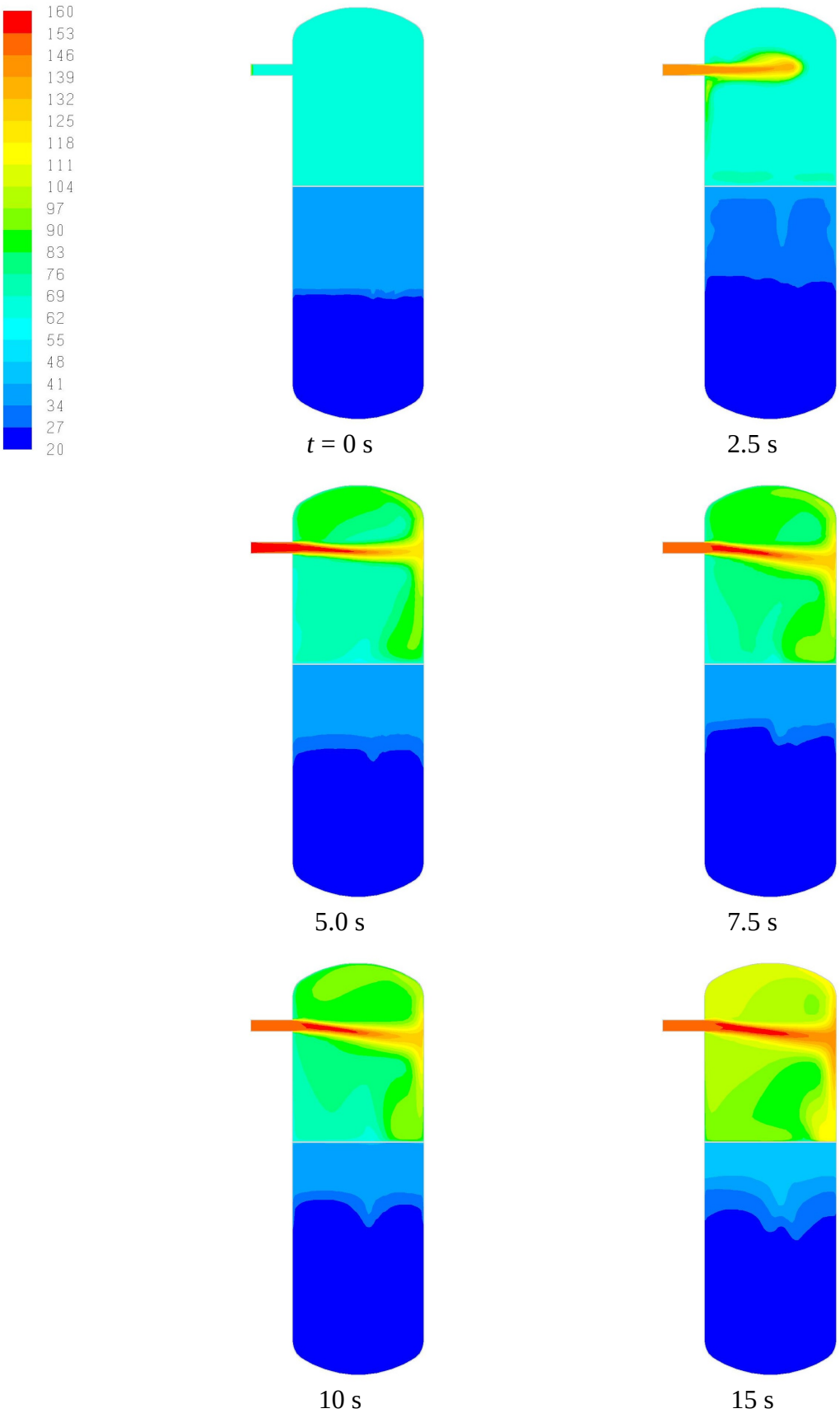

Figure 6. Temperature of gas (C) in the central cross-section at different instants of time.

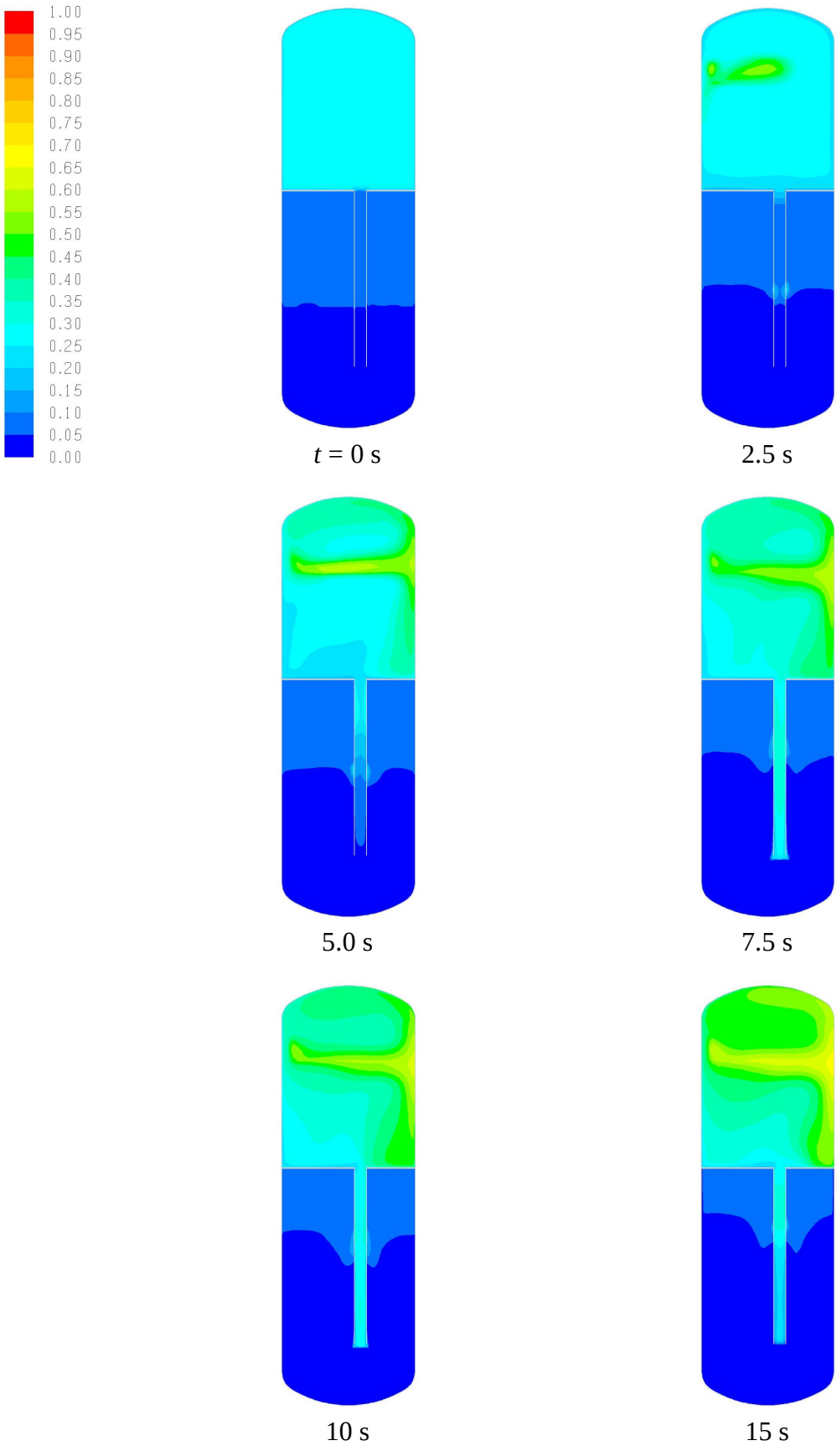

Figure 7. Mole fraction of vapor in the vent cross-section at different instants of time.

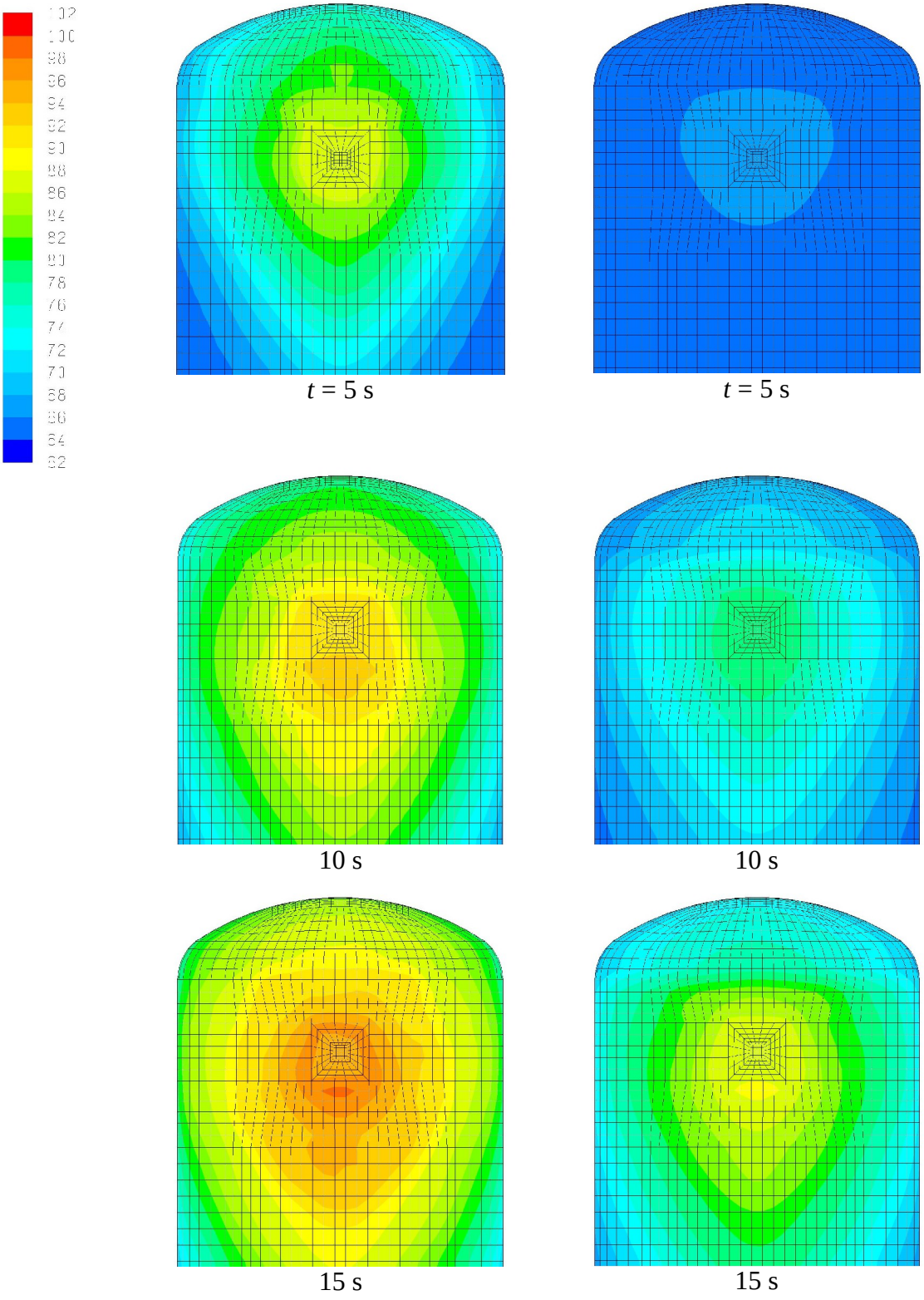

Figure 8. Temperature (C) of the inner (lef-hand side) and outer (right-hand side) wall of the drywell opposite to the inlet plenum.

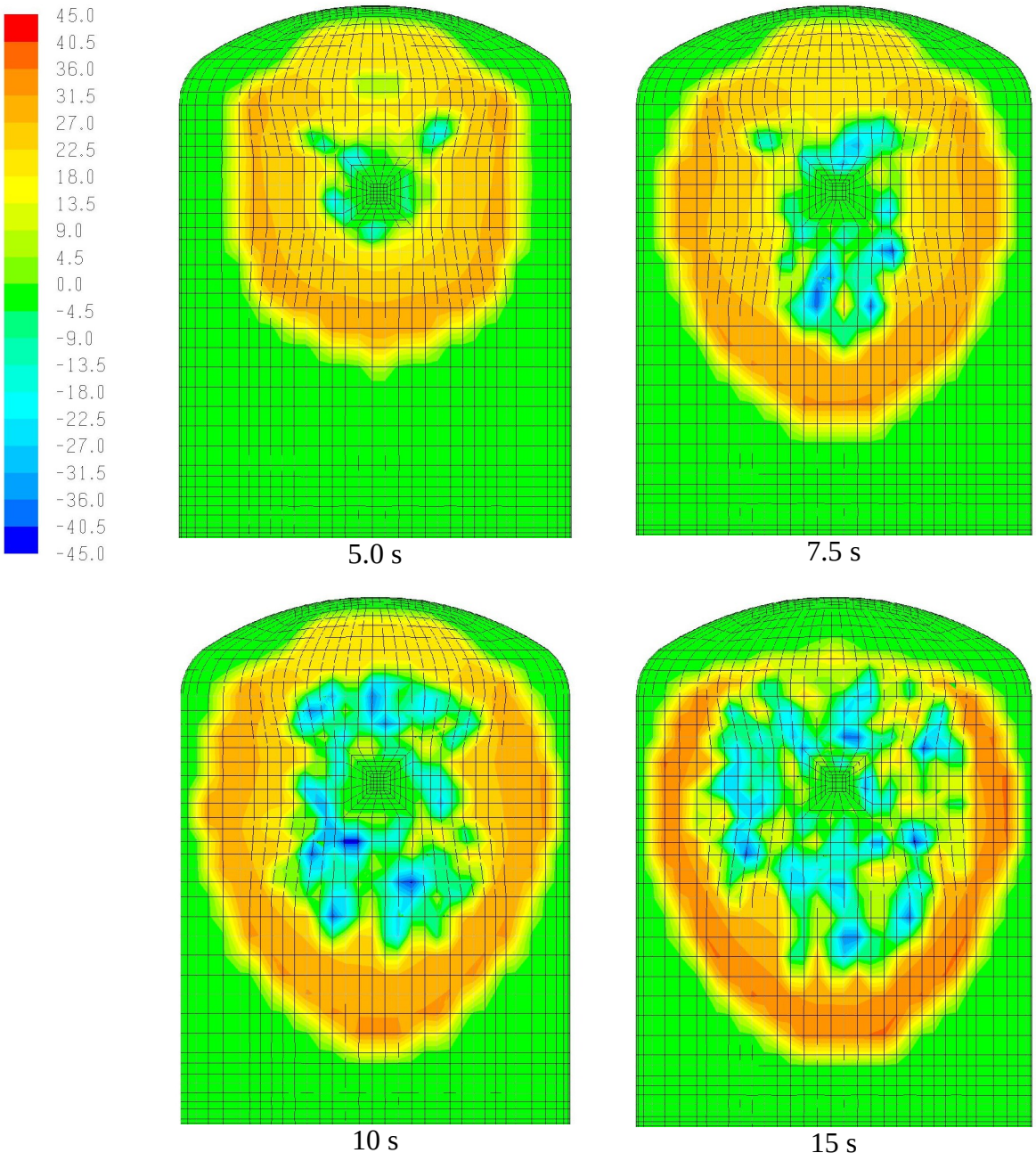

Figure 9. Mass transfer rate (kg/m^{2}s) between the gas and liquid phases in wall condensation.

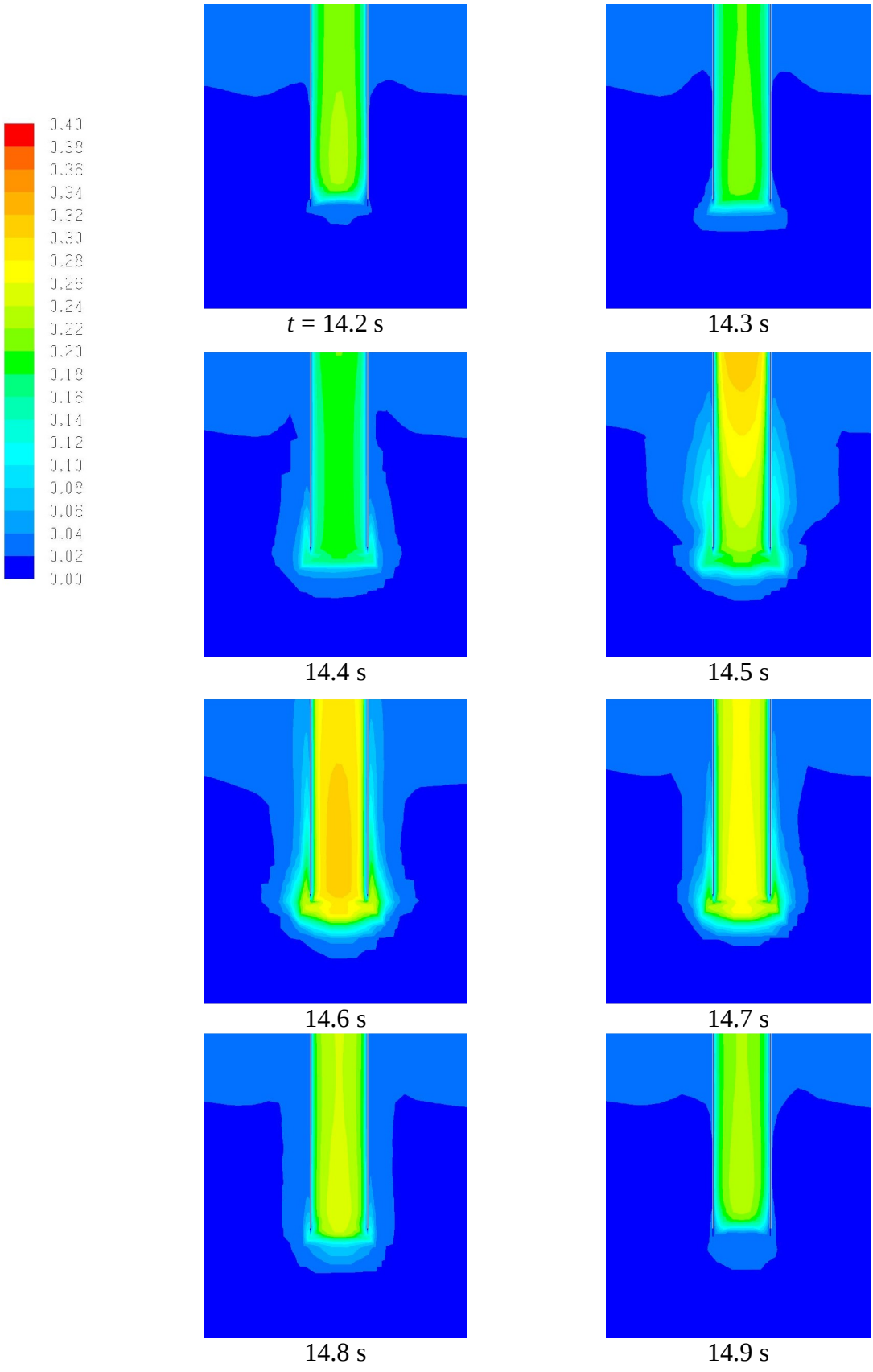

Figure 10. Mole fraction vapor at the outlet of the vent pipe during formation of a bubble.

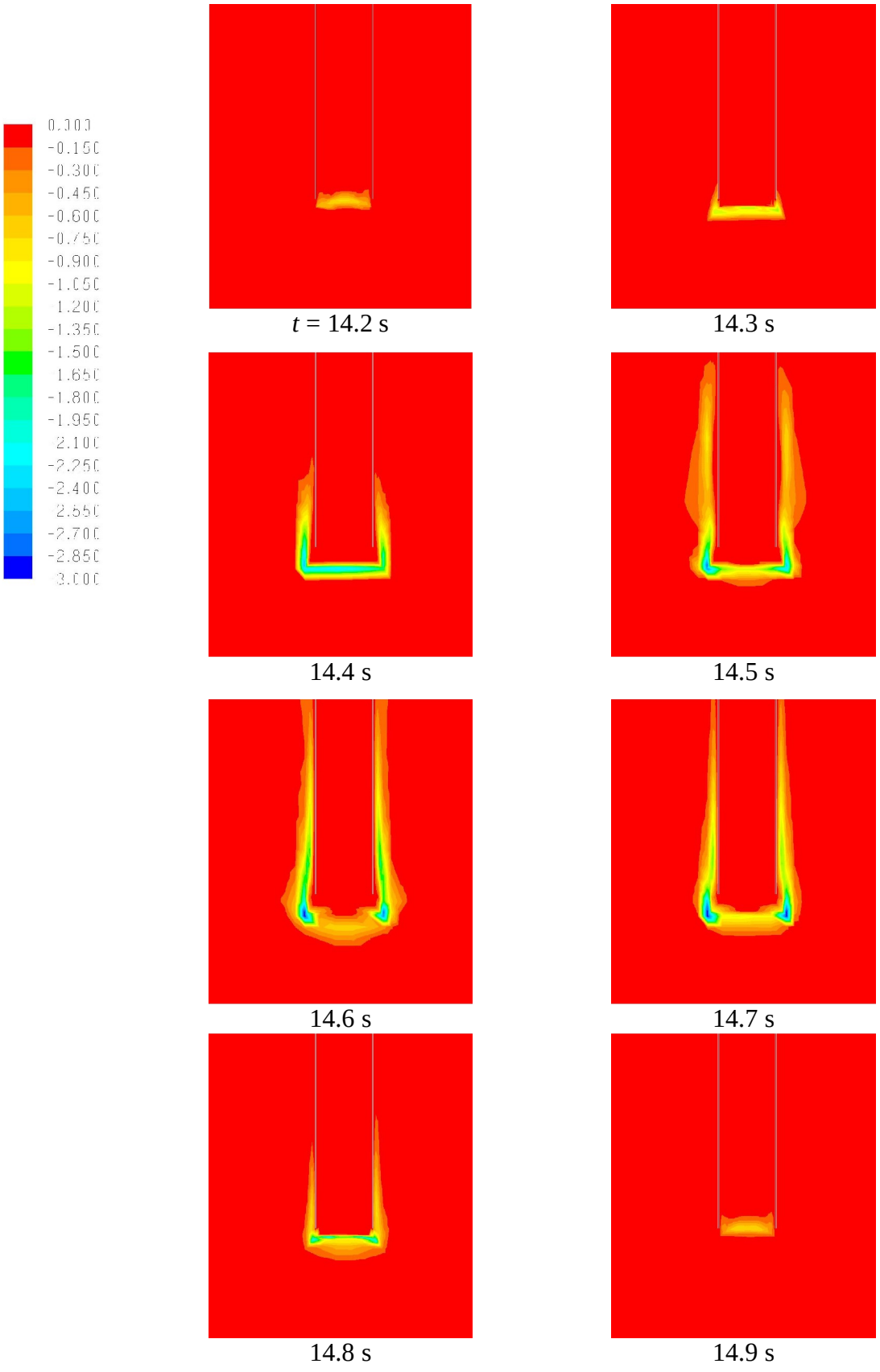

Figure 11. Mass transfer rate (kg/m^{3}s) between gas and liquid phase during direct-contact condensation at the outlet of the vent pipe.

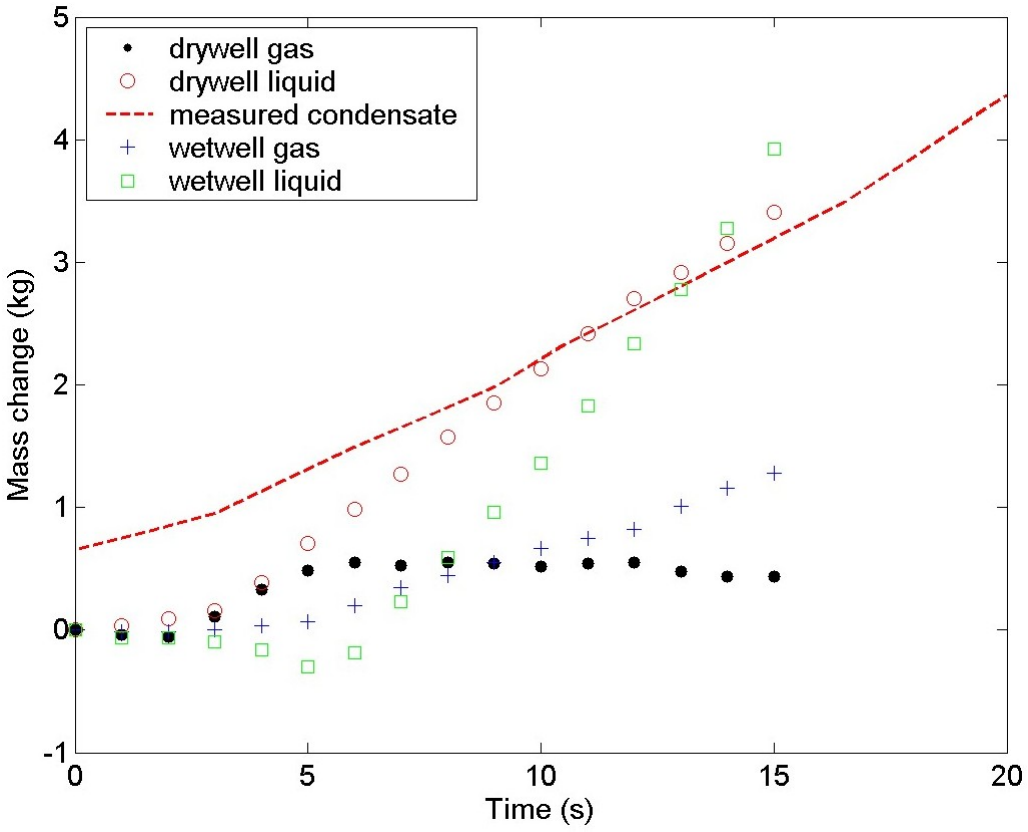

Figure 12.Comparison of measured amount of condensate in the drywell in the experiment WLL-05-02 and in the CFD simulation.

In figure 7, the mole fraction of vapor in the gas phase is shown during the early part of the discharge. It is seen that at time t = 15 s, a considerable amount of non-condensable air still exists in the drywell. The mole fraction of vapor varies from 0.3 to the value 0.98 of the incoming vapor jet. Therefore, non-condensable air strongly affects the direct-contact condensation in the water pool even at the end of the present simulation.

In figure 8, the temperature of the inner and outer wall of the drywell is shown in the region opposite to the inlet plenum. The wall is strongly heated by the vapor jet hitting the inner wall. The temperature of the outer wall increases with a delay determined by the heat conduction through the 10 mm steel wall of the drywell. The inner and outer wall temperatures have the maximum values of T = 100 °C and T = 90 °C at time t = 15 s, respectively.

In figure 9, the wall condensation of vapour is shown on the wall of the drywell opposite to the inlet plenum. When vapour jet hits the wall at the so-called stagnation point, it turns 90 degrees and flows along the wall away from the stagnation point. Condensation is strongest around the stagnation point, where the mass transfer rate between the phases has negative values. When the vapour jet hits the water film, hot water splashes away from the stagnation point. Therefore, later some evaporation of hot water occurs around the stagnation point, where the

mass transfer rate between the phases has positive values. Some more detailed validation of this behaviour of condensation and evaporation against experimental data would be necessary. In the present experiment, however, comparison of the amount of the condensate in the experiment and simulation is only possible.

In figure 10, the mole fraction of vapor is shown in the water pool near the outlet of the vent pipe. The chosen time interval between 14 and 15 s corresponds to the last bubble of the present simulation. At this time, the mole fraction of vapor was largest during the present simulation because part of the air originally in the drywell had already flown into the wetwell. The mole fraction of vapor has the maximum value of about 0.3 at time t = 14.6 s because then the flow rate through the vent pipe has its maximum value. Note that strong wall condensation also occurs in the vent pipe submerged into the water pool. The wall condensation is clearly manifested by the low mole fraction of vapor near the inner wall of the vent pipe.

In figure 11, the mass transfer rate in direct-contact condensation is shown at the outlet of the vent pipe. The condensation is strongest at time t = 14.6 s, when the flow rate through the vent pipe has its maximum value. The large fraction of non-condensable gas strongly limits the amount of direct-contact condensation still at this time.

In figure 12, the total amount of condensate in the drywell during the experiment WLL-05-02 has been plotted. The condensate is collected with an aqueduct system mounted on the walls of the drywell. Therefore, some delay is inevitable before the condensate flows into the tanks, where its weight is measured as a function of time. We have therefore shifted the time scale of the measurement in order to take into account a delay of 30 s in the measurement. The measured amount of condensate is compared to the calculated amount of liquid in the drywell. The calculated amount of condensate is found to be approximately correct. In addition, the calculated rate of condensation at the end of the simulation seems to correspond approximately to the experimental result. However, more simulations are necessary in order to obtain more detailed comparison of the simulations and experiments.

5 Fluid-structure interaction calculations

A linear perturbation method (LPM) for circumventing the instability has been developed and examined in the earlier work (Timperi et al., 2007; Pättikangas et al., 2008) and in Huber et al. (1979) and Sonin (1980). The method consists of the following:

- An acoustic-structural FEM model. The fluid is modelled as an acoustic medium and the acoustic pressure and displacement have two-way coupling.
- CFD model of the fluid problem.
- One-way coupling of the CFD and FEM models, i.e. only pressure load is transferred from the CFD model to the FEM model.

In the method, pressure load is transferred from the CFD model to the structural model, but no displacement feedback is send back. Mass of the fluid is accounted for in the structural motion through the separate acoustic fluid which has two-way coupling with the structure. The method eliminates the numerical instability as the coupling between CFD and structural models is only one-way. A stable monolithic approach is used for the acoustic-structural system, see e.g. Cook et al. (2002).

Basis of the method and its validity for modeling condensation pools have been examined mathematically with an order of magnitude analysis. The method becomes invalid for sufficiently high flow velocity near moving walls, but it remained to be fully shown whether it suffices that flow velocity stays moderate only near the walls. During blowdown, flow velocity in the pool is generally small near walls but can be relatively large near the pipe outlet. Further validation against numerical and experimental data is conducted in the following.

5.1 Calculations with axisymmetric model

A simple axisymmetric model of the PPOOLEX facility, shown in Fig. 13, was first used. The pool has rigid side wall and a bottom plate that experiences only vertical rigid-body motion. This kind of system resembles the real pool in that the most dominant mode is the vertical oscillation of the whole pool (Pättikangas et al., 2008). A harmonic pre-determined wall motion is assumed for the bottom plate so that the numerical instability is prevented in moving-mesh CFD calculations.

Aim of the calculations is to test LPM with different parameters, such as blowdown velocity and amplitude of the wall motion. In particular, we study the interaction of the two flow components: flow if the walls were perfectly rigid and flow due to wall motion. LPM requires that there is practically no interaction so that the two flow fields can be superposed (Timperi et al., 2007; Pättikangas et al., 2008).

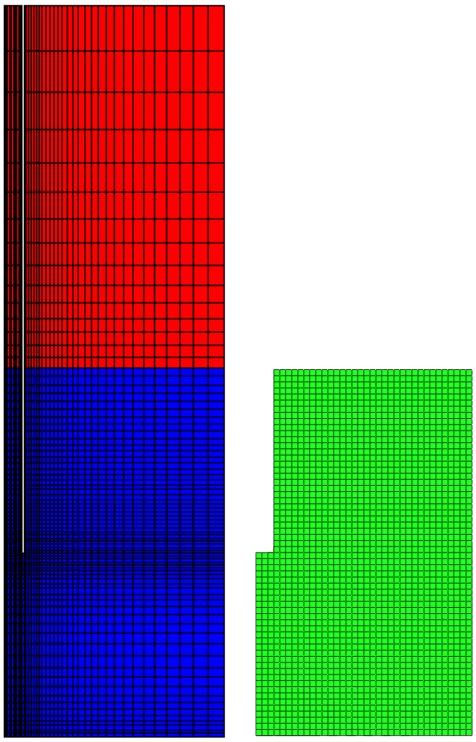

Figure 13. Axisymmetric CFD (left) and acoustic (right) models of the PPOOLEX facility.

5.1.1 VOF calculations

Beginning of the blowdown, i.e. when the water plug is expelled from the pipe, is considered in this section. Frequency and amplitude of the wall motion are set to 10 Hz and 1 mm which are close to the values observed in the experiments (Laine and Puustinen, 2008). The VOF model is used for tracking the free surface and both air and water are assumed incompressible. Turbulence is modelled with the k-ε model. Constant flow velocity of 20 m/s is used at the blowdown pipe inlet which is of the same order as in the experiments. Also conservative wall amplitude of 10 mm and blowdown velocity of 100 m/s are tested.

Fig. 14 shows volume fraction of water in the pool at different instants of time with blowdown velocity 10 m/s. Pressures at the pool bottom are compared in Figs. 15 and 16. Pressures obtained from the moving-mesh calculation and with LPM are in good agreement. The calculation with rigid walls shows only the blowdown load, i.e. the effect of wall motion on the pressure is not included. LPM becomes invalid for sufficiently high flow velocity near moving walls. During blowdown, flow velocity in the pool can be relatively large near the pipe outlet but in these calculations validity of the method is unaffected by this. Furthermore, the method works well in this kind of case although the free surfaces of the acoustic fluid remain static during the calculation.

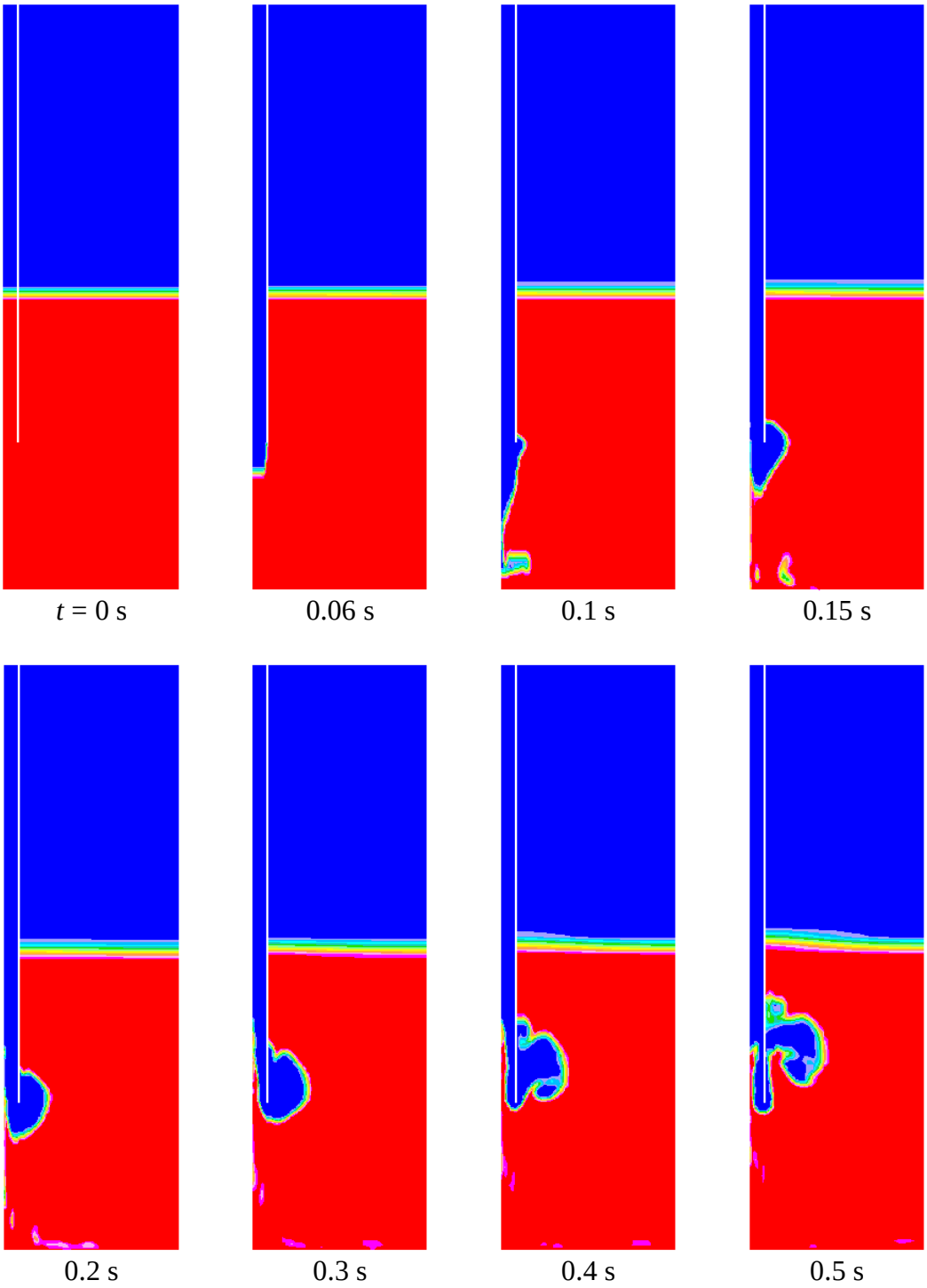

Figure 14. Volume fraction of water in a calculation with axisymmetric model.

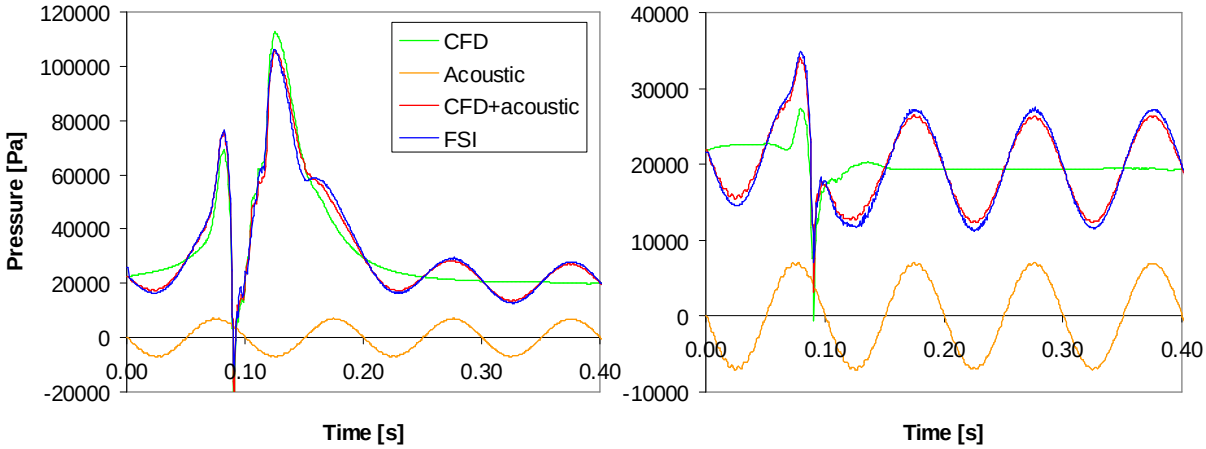

Figure 15. Wall pressure below pipe (left) and average wall pressure (right) in VOF calculation with axisymmetric model. Inlet velocity and wall amplitude were 20 m/s and 1 mm.

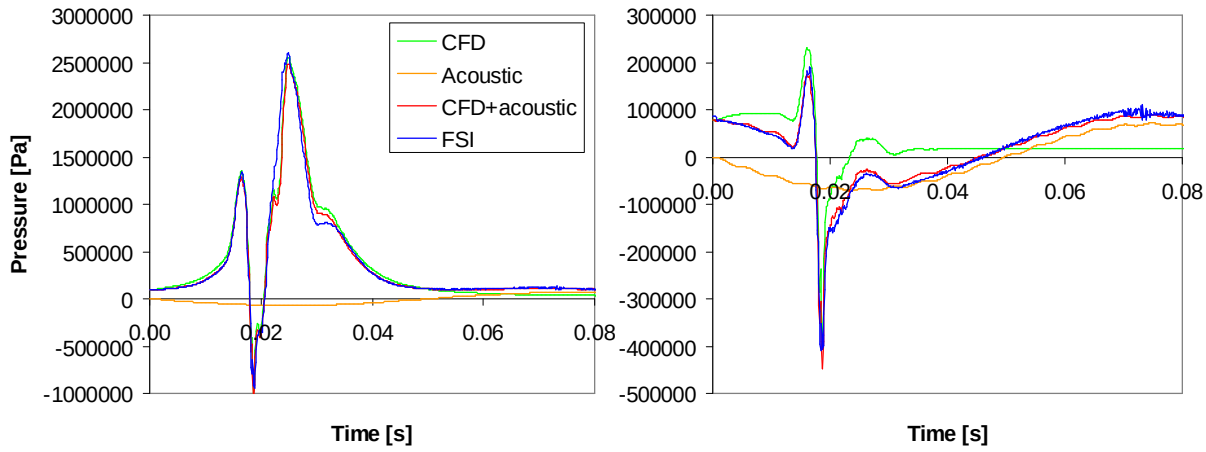

Figure 16. Wall pressure below pipe (left) and average wall pressure (right) in VOF calculation with axisymmetric model. Inlet velocity and wall amplitude were 100 m/s and 10 mm.

5.1.2 Single-phase calculations

The chugging phase is considered in this section. The pool is assumed to be completely filled with water and a harmonic velocity variation is applied at the blowdown pipe inlet. This kind of calculation resembles the chugging phase where a water column oscillates back and forth in the blowdown pipe. Amplitude of the velocity boundary condition is 10 m/s and frequencies 1 and 4 Hz are tested. Amplitude and frequency of the wall motion are set to 1 mm and 10 Hz. Water is assumed incompressible and turbulence is modelled with the *k-ε* model.

Fig. 17 shows velocity fields from the calculation with velocity boundary condition frequency of 1 Hz. It is seen that water jets issue periodically from the blowdown pipe and impact on the pool floor. Video recordings of chugging show similar jets in the experiments. The different pressure components at the pool

floor are presented in Figs. 18 and 19. It is seen that also in this case the assumption of linear superposition of the two components is well justified, i.e. the sum of these and the pressure obtained from taking FSI fully into account coincide.

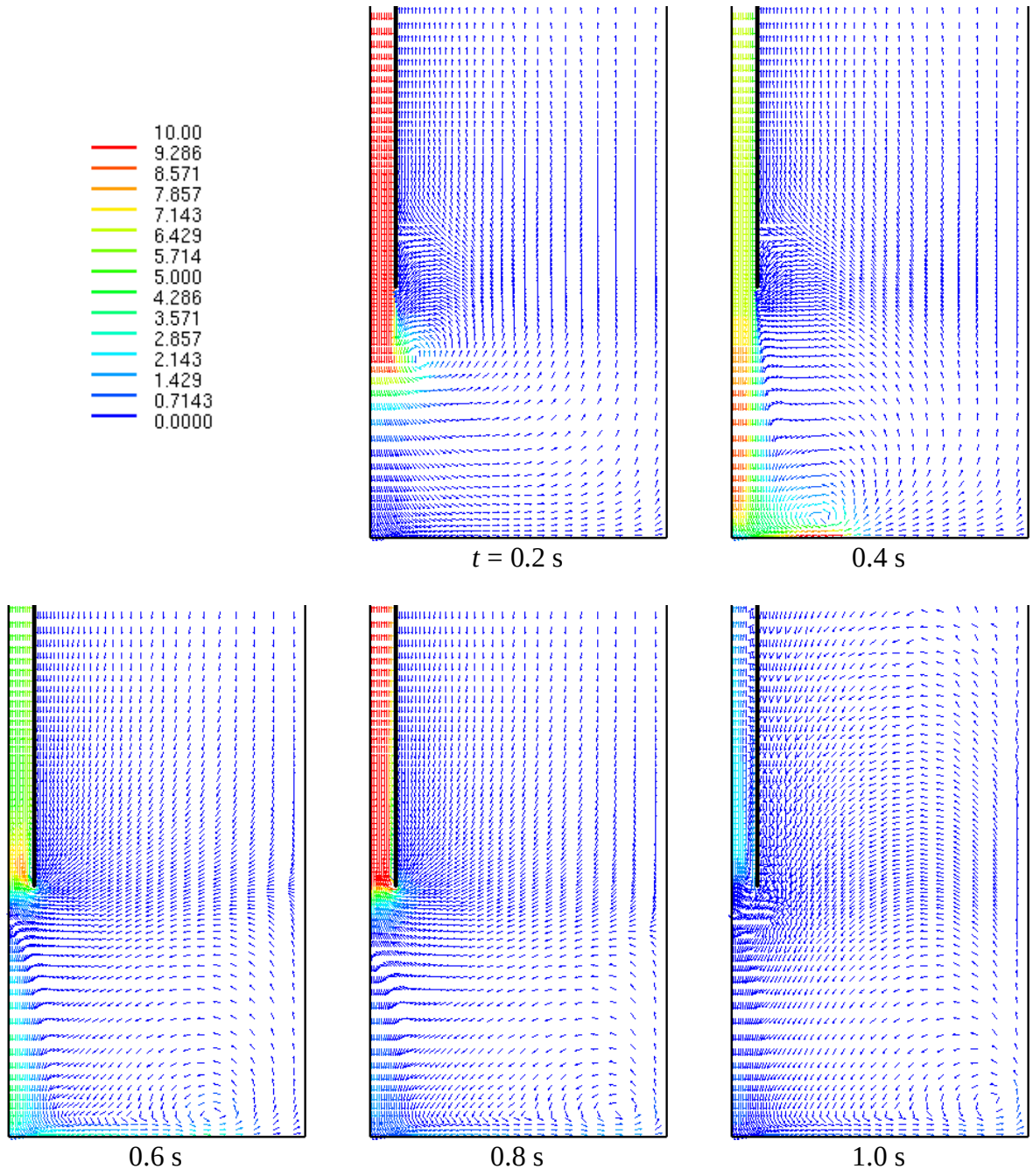

Figure 17. Velocity field at different instants of time in a single-phase calculation with axisymmetric model.

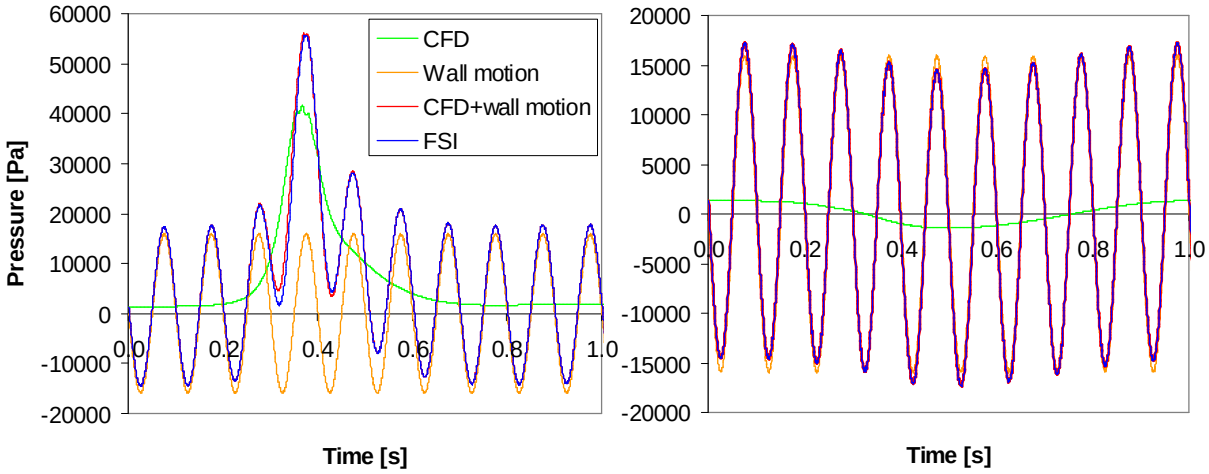

Figure 18. Wall pressure below pipe (left) and average wall pressure (right) in single-phase calculation with axisymmetric model. Frequency of inlet velocity was 1 Hz.

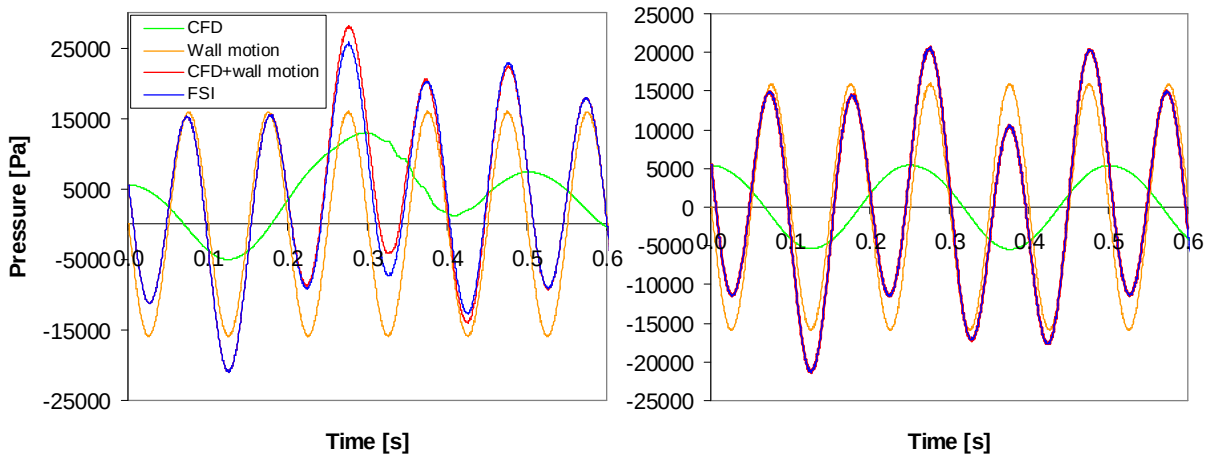

Figure 19. Wall pressure below pipe (left) and average wall pressure (right) in single-phase calculation with axisymmetric model. Frequency of inlet velocity was 4 Hz.

5.2 Calculation of PPOOLEX experiment SLR-05-02

Numerical models used for the FSI calculations are presented in Fig. 20. The CFD mesh has about 135 000 hexahedral cells. For the structure, a fairly detailed FEM model consisting mainly of about 15 000 4-noded shell elements was used. Flexibility of disc springs and structures under the four vertical support columns were modeled with linear springs. The VOF and k-ε models were used in the CFD calculation. Air was treated as ideal gas and a logarithmic equation of state suitable for compressible liquids was used for water. Mass flow at the drywell inlet was set according to the measured mass flow curve shown in Fig. 21.

Charging of the drywell with air was found to be significantly slower in the calculation which is probably caused by delay in the mass flow sensor (Puustinen, 2008). Flow of air in the experiment was probably larger, or at least raised faster, than shown in Fig. 21. The first bubble appeared at the blowdown pipe outlet at t = 1.5 and t = 3.4 s in the experiment and simulation, respectively. A similar

PPOOLEX experiment CHAR-09-04, where the mass flow curve was close to that in Fig. 21, was calculated by Pättikangas et al. (2008) with the Fluent code. In that calculation, the first bubble appeared at t = 3 s and significant delay in the charging of the drywell was found compared to the experiment. In the following, times between the simulation and experiment have been synchronized to the moment when the first bubble appears.

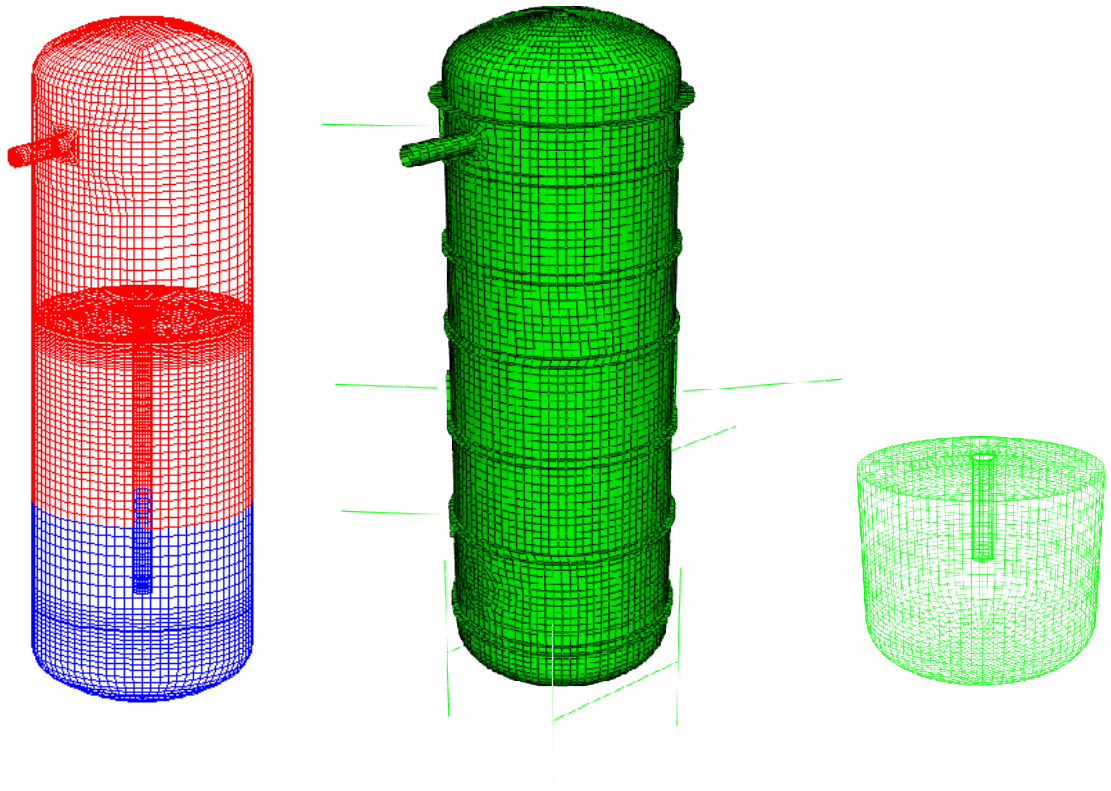

Figure 20. Numerical meshes of the PPOOLEX facility. From left to right: CFD, structural and acoustic model.

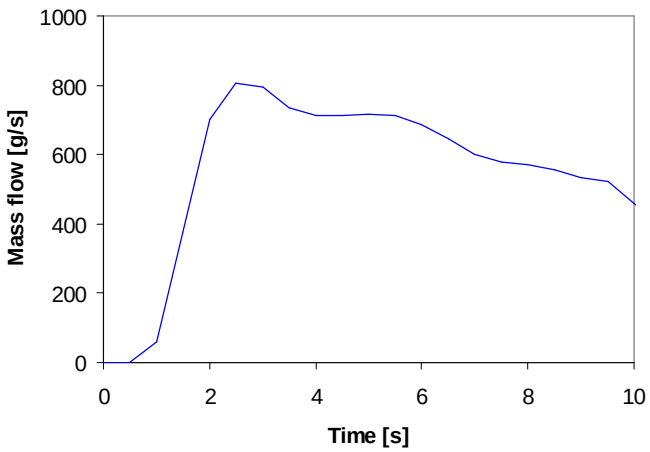

Figure 21. Mass flow of air measured at the drywell inlet in PPOOLEX experiment SLR-05-02.

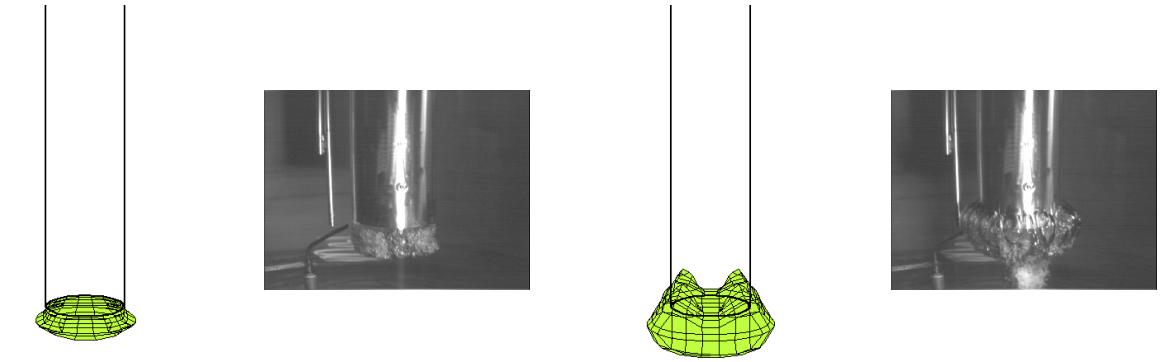

t = 1.53 s 1.63 s

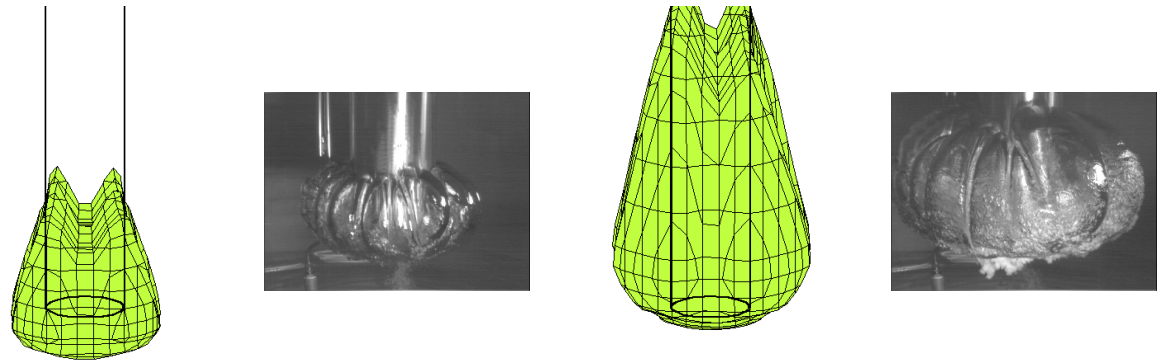

1.74 s 1.84 s

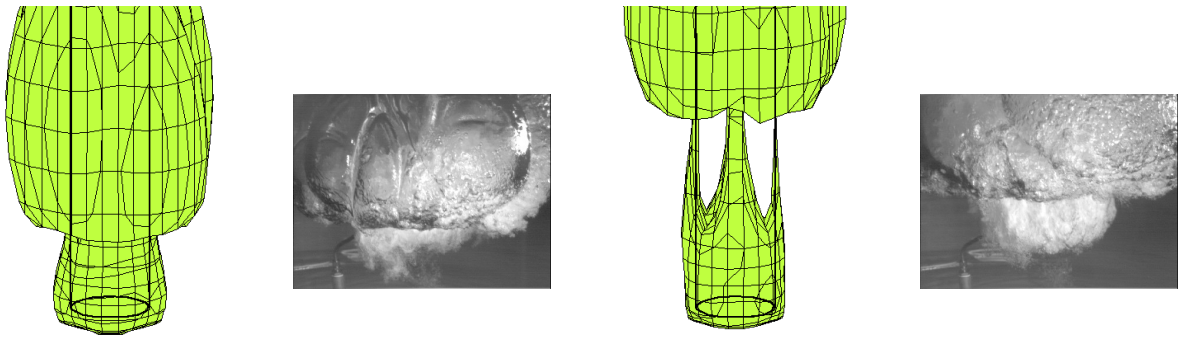

1.94 s 2.04 s

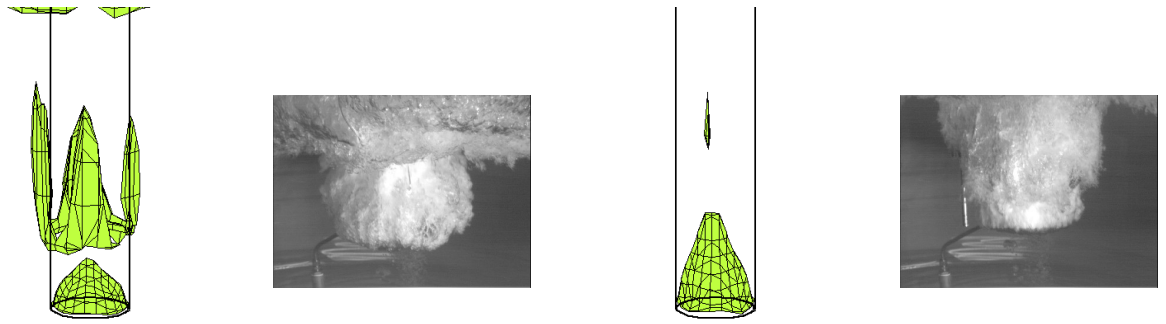

2.14 s 2.24 s

Figure 22. Water surface at different instants of time in simulation and in PPOOLEX experiment SLR-05-02.

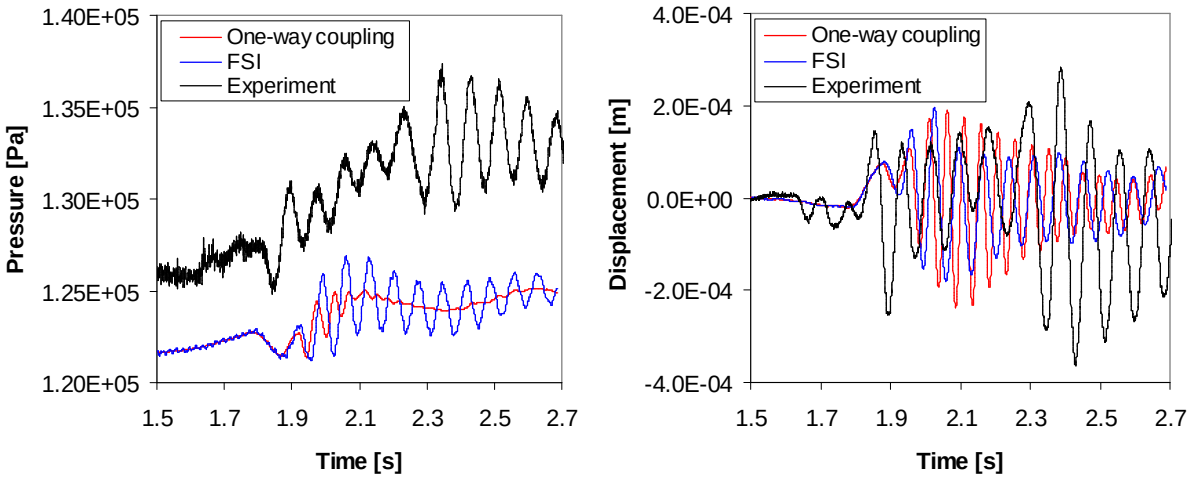

Figure 23. Pressure and displacement at pool bottom in simulation and in PPOOLEX experiment SLR-05-02.

Bubble shapes at the pipe outlet are compared in Fig. 22. Pressure and displacement at the pool bottom are presented in Fig. 23. The calculation with FSI shows qualitatively correct results. The wall pressure can be in this case separated into two components: fluid-dynamic load caused by the blowdown and pressure due to wall motion. The pressure load is expected to be somewhat smaller in the calculation due to the lower amount of air injected into the drywell. Amplitude and frequency of the pool motion is similar in the experiment and calculations. The frequency is similar with or without FSI because structures of the PPOOLEX facility have almost the same mass as the pool water.

5.3 Calculation of POOLEX experiment STB-17-6

In the following, we consider experiment STB-17-6 where steam was blown into the pool. The numerical models are presented in Fig. 24. Aim was to simulate only the beginning phase where clearing of the blowdown pipe from water causes a pressure load on the pool bottom. The both fluids were assumed incompressible and velocity was fixed to 15 m/s at the pipe inlet. This value was estimated from high-speed video frame captures shown in Fig. 25.

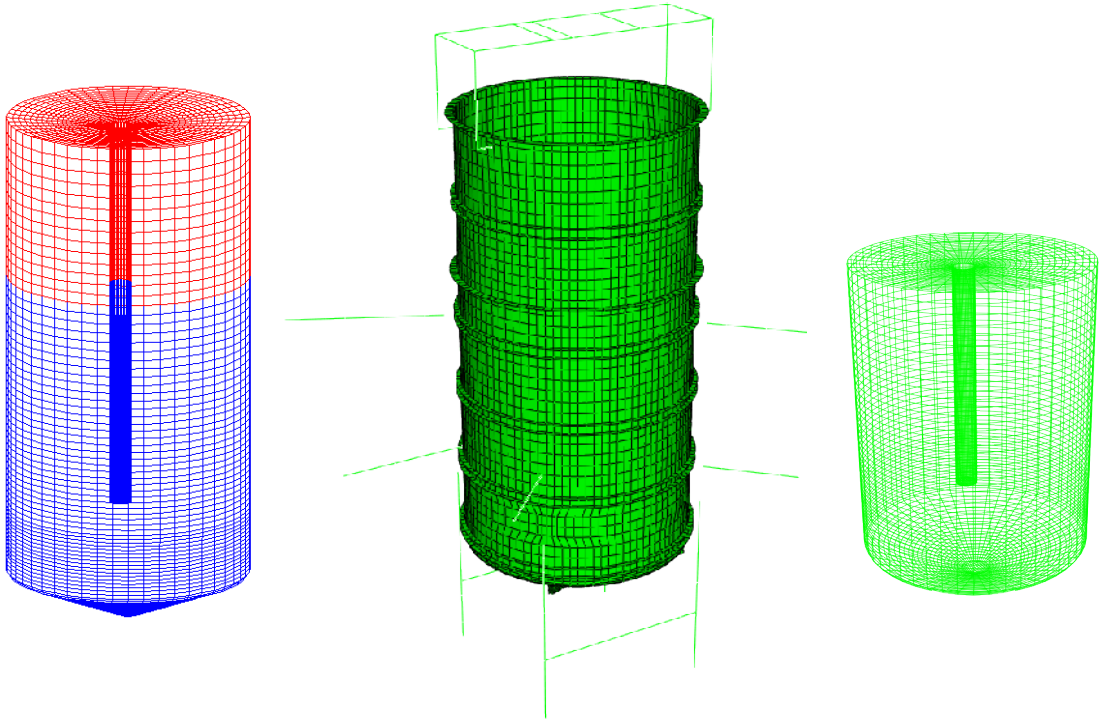

Figure 24. Numerical meshes of the POOLEX facility. From left to right: CFD, structural and acoustic model.

Location of water surface at selected instants of time in the simulation is presented in Fig. 26. Pressure and stress at the pool bottom are presented in Figs. 27 and 28. Note that the times between the simulation and experiment have been synchronized to the moment when the first bubble appears. Compared to calculations presented in the previous section, these show much larger added mass effects due to the relatively light pool structures. Condensation of steam in the considered experiment was not modelled which could explain the significantly higher pressure load and stresses in the experiment. The calculations show, however, that FSI has to be accounted for.

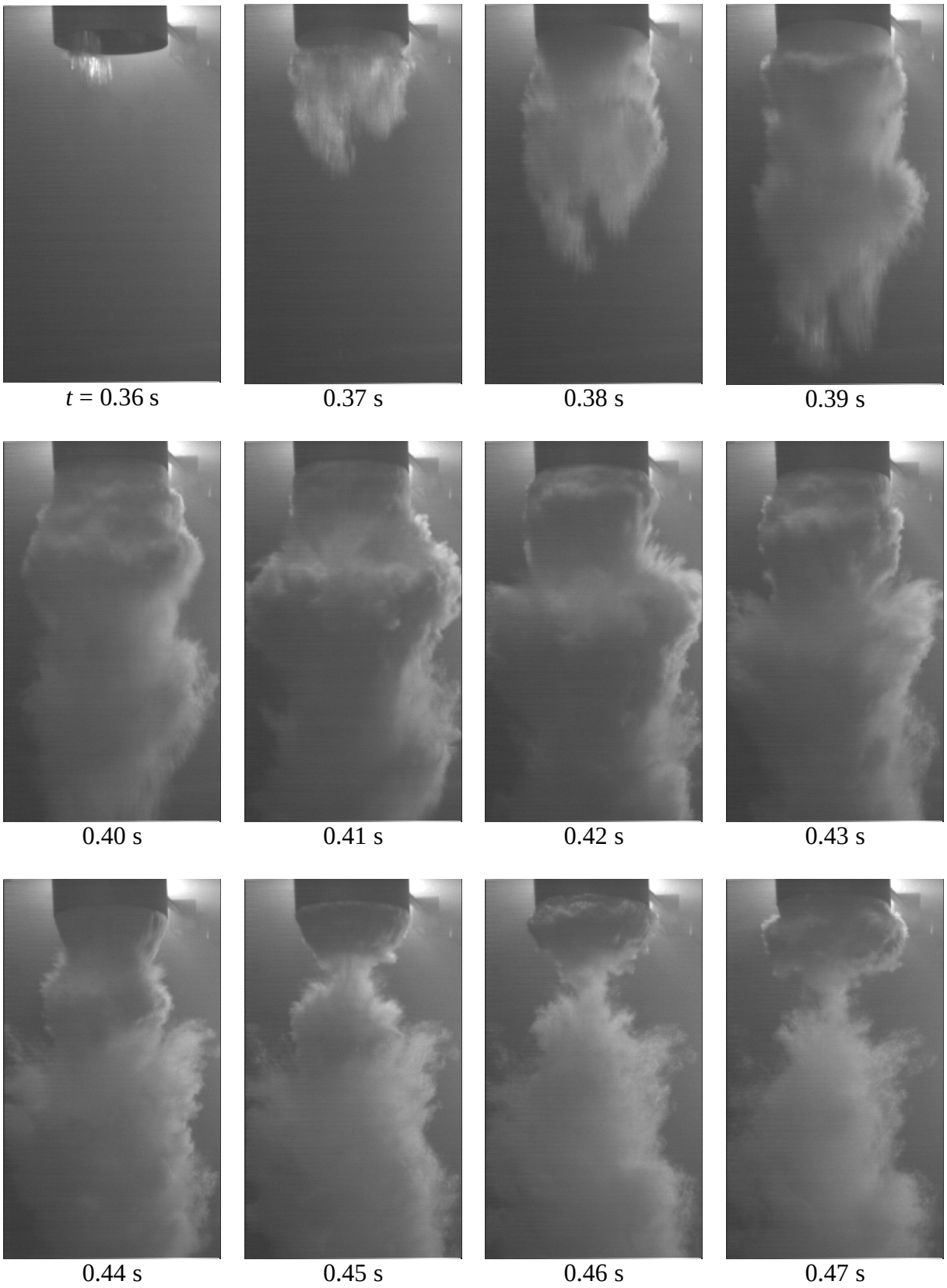

Figure 25. Frame captures from POOLEX experiment STB-17-6.

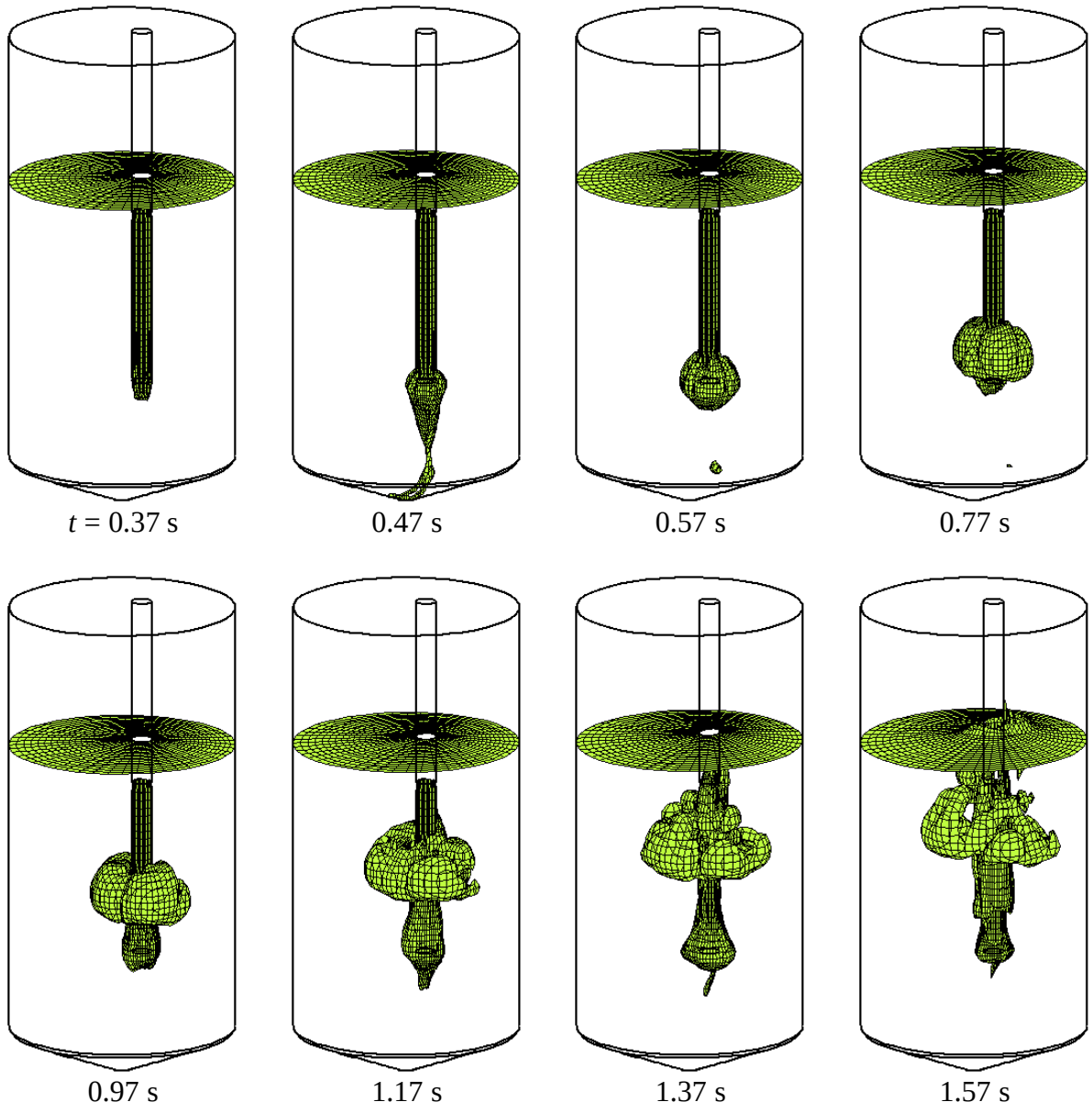

Figure 26. Water surface at different instants of time in simulation of POOLEX experiment STB-17-6.

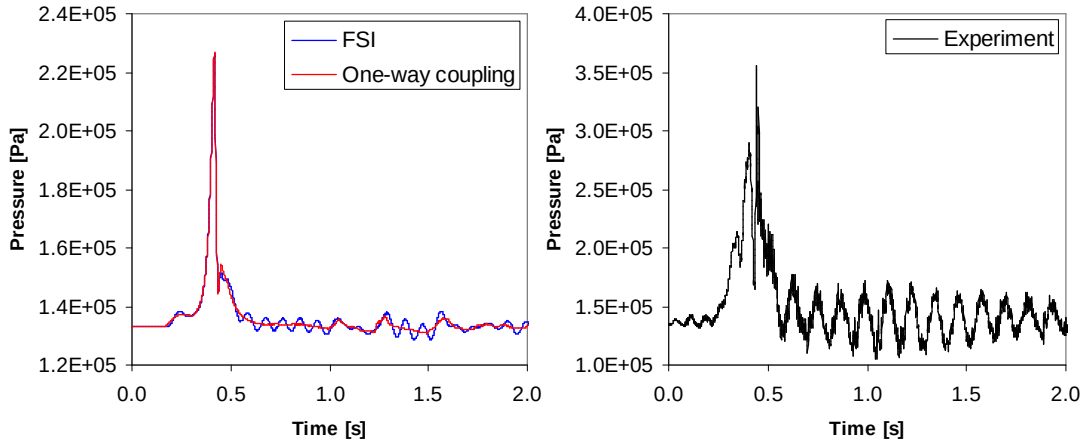

Figure 27. Pressure at pool bottom in POOLEX experiment STB-17-6.

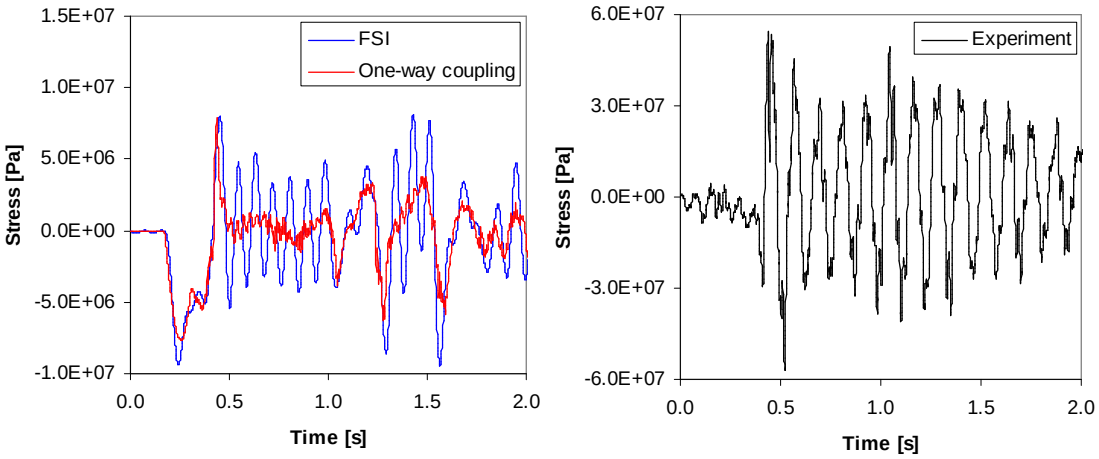

Figure 28. Stress at pool bottom rounding in POOLEX experiment STB-17-6.

6 Determination of the pressure source

Determination of the pressure source from pressure signal at the pool bottom is in principle fairly straightforward, but also the wall motion affects the measured pressure. For the POOLEX and PPOOLEX experiments, pressure at the pool bottom can be separated into the following components (Timperi et al., 2007; Pättikangas et al., 2008):

$$p(t) = p(t)_{load} + p(t)_{wall\_motion} \tag{20}$$

where $p(t)_{load}$ is pressure caused by the blowdown load and $p(t)_{wall\_motion}$ is pressure caused by the resulting wall motion. In other words, $p(t)_{load}$ would be the measured pressure if the pool walls were perfectly rigid. We would like to know the pressure due to wall motion so that the actual blowdown load could be evaluated:

$$p(t)_{load} = p(t) - p(t)_{wall\_motion} \tag{21}$$

The pressure due to wall motion is caused essentially by wall acceleration. This pressure component has therefore been significant in the experiments although the wall displacement has been relatively small. If we assume incompressible water and only vertical oscillation of the whole pool, which is predominantly the case for the PPOOLEX facility, the pressure caused by wall motion at pool bottom is

$$p(t)_{wall\_motion} = \rho \ddot{x} h \qquad (22)$$

where ρ is water density, $\ddot{x}$ is vertical acceleration of the pool and h is water level. For compressible water, i.e. high-frequency wall motion, and/or more complicated geometry, the acoustic FEM model can be used for analyzing this pressure component (Pättikangas et al., 2008). Using Eq. (22) may be sufficient for the POOLEX and PPOOLEX experiments.

6.1 Fourier analysis of measured displacement

Determining the acceleration by differentiating numerically the displacement signal is inaccurate. Circumvention of this issue is attempted in the following by conducting the Fast Fourier Transform (FFT) to the measured displacement signal. The separate Fourier components are then differentiated analytically twice and summed over some frequency range. This kind of procedure might produce accurate enough acceleration signal. Signal on which the procedure is tested is shown in Fig. 29, namely displacement measured from the pool bottom centre in PPOOLEX experiment SLR-05-02. FFT is conducted by using the Matlab software.

Fig. 30 shows the Fourier spectrum of the wall motion obtained by conducting FFT for two different time intervals. The most dominant mode of oscillation is the vertical motion of the whole pool at about 11.7 Hz. This is due to springs under the four support legs of the pool and possibly also due to flexibility of the base structure (Pättikangas et al., 2008; Laine and Puustinen, 2008).

Displacement and acceleration signals obtained from the analysis are shown in Figs. 31 - 33. Fourier components have been summed from the lowest one up to some cutoff frequency. From Fig. 31 it is seen that the original signal is not very well reproduced. At some time instants, the original and transformed signals have opposite phases. Sensitivity of the results on the interval for which FFT is conducted is shown in Fig. 33 for the acceleration. It would be particularly important to get the phase correctly but this is not achieved.

Subtracting the pressure fluctuations due to wall motion from the measured pressure using acceleration from FFT was briefly tested. Figs. 34 and 35 show pressure measured from the pool bottom in the considered experiment and pressures obtained by low-pass filtering the original signal. Fluctuations caused by the wall motion are mainly seen in the filtered signals. Figs. 36 and 37 show the pressures obtained from Eq. 21. As was expected from the transformed displacement and acceleration signals, accurate enough results can not be obtained this way.

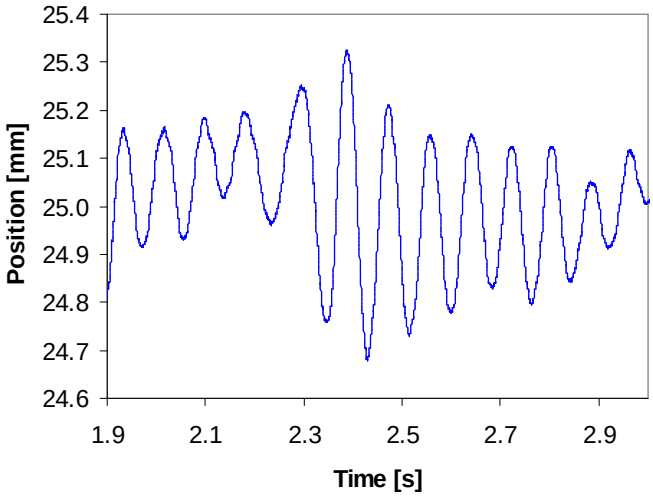

Figure 29. Vertical motion of the pool bottom measured in PPOOLEX experiment SLR-05-02.

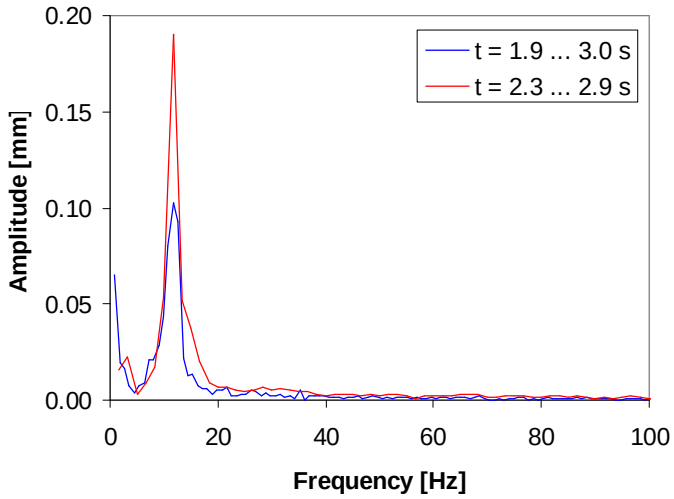

Figure 30. Spectrum for the measured displacement determined from two different time intervals.

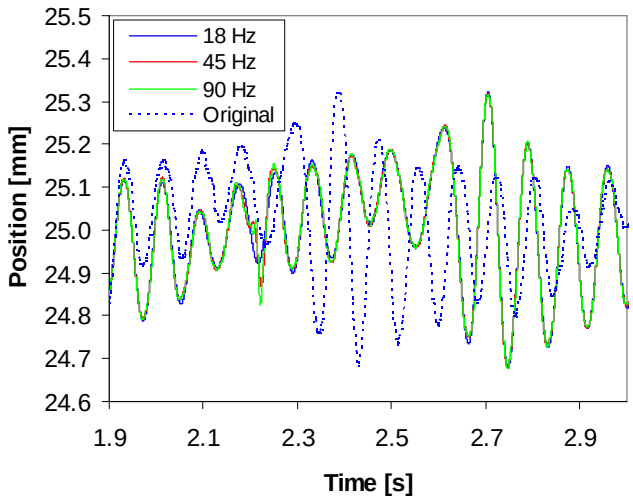

Figure 31. Measured displacement and displacements obtained from FFT with different cutoff frequencies.

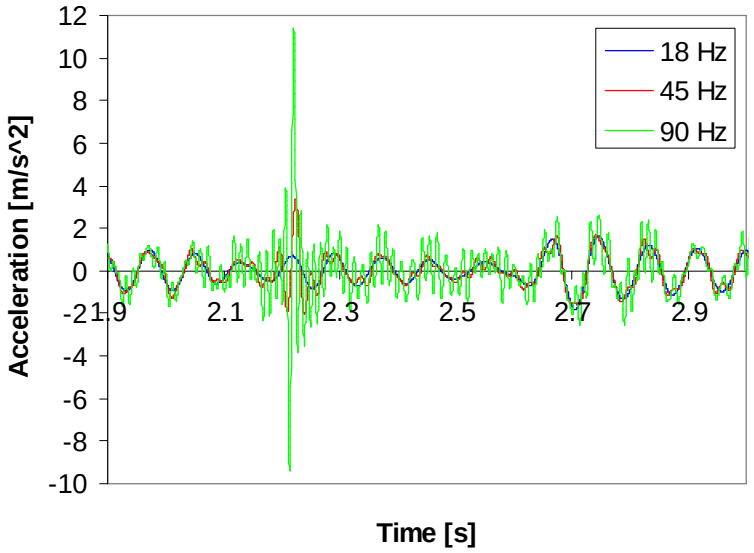

Figure 32. Acceleration obtained from FFT of the measured displacement with different cutoff frequencies.

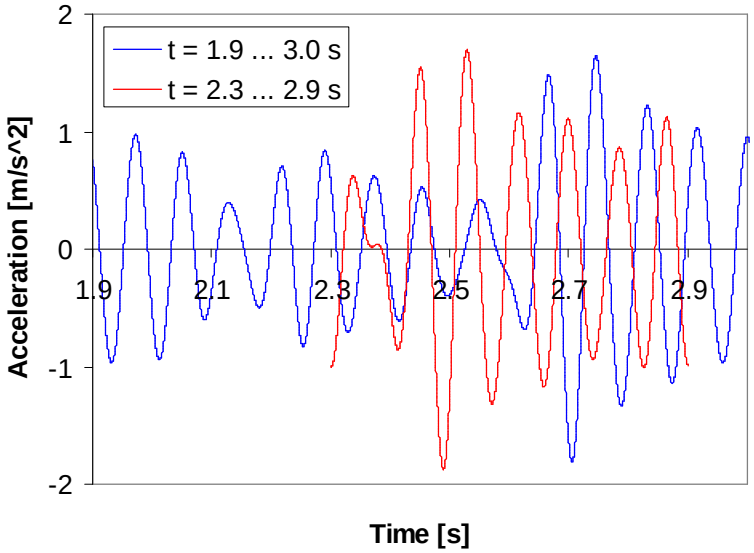

Figure 33. Acceleration obtained from FFT of the measured displacement using two different time intervals. The cutoff frequency is approximately 18 Hz.

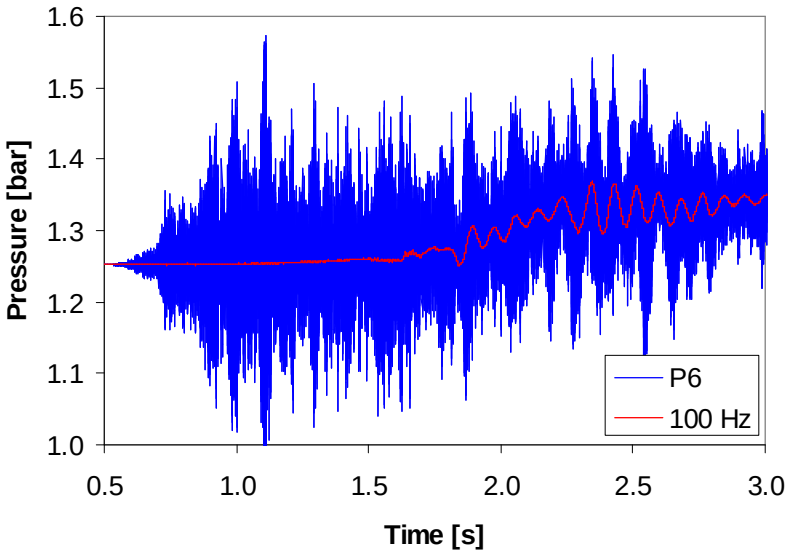

Figure 34. Pool bottom pressure measured in PPOOLEX experiment SLR-05-02 and its filtered signal with cutoff frequency 100 Hz.

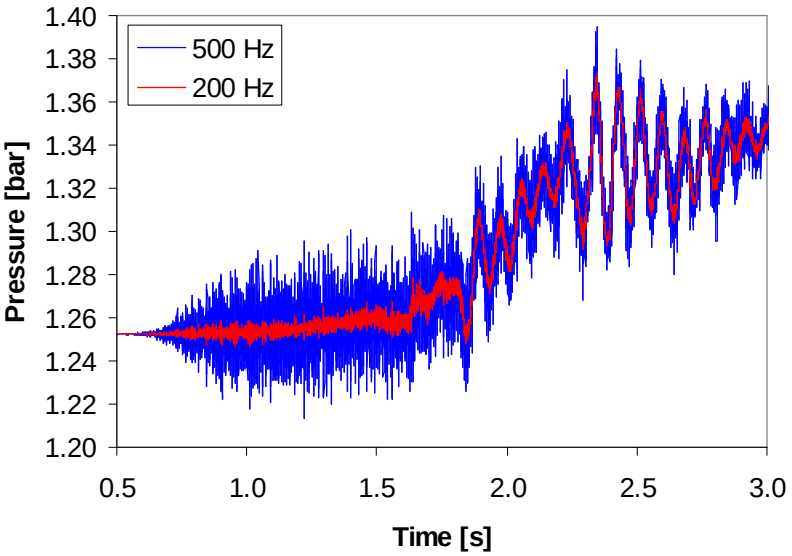

Figure 35. Filtered signal of the measured pool bottom pressure with cutoff frequencies 200 and 500 Hz.

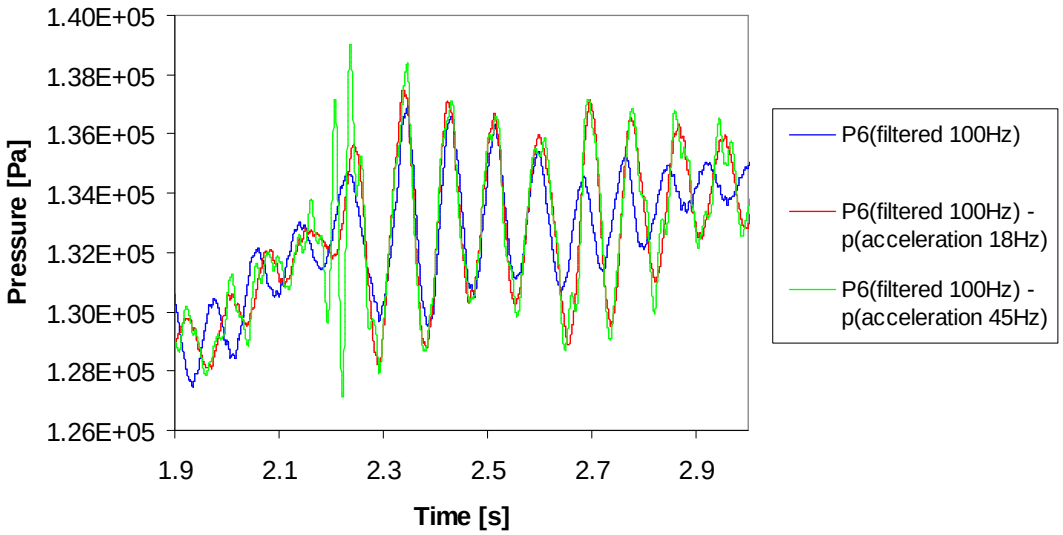

Figure 36. Filtered pool bottom pressure and pressures obtained by subtracting the effect of wall motion. Cutoff frequencies used in FFT and in filtering are shown in the legend. Time interval 1.9 … 3 s was used in FFT.

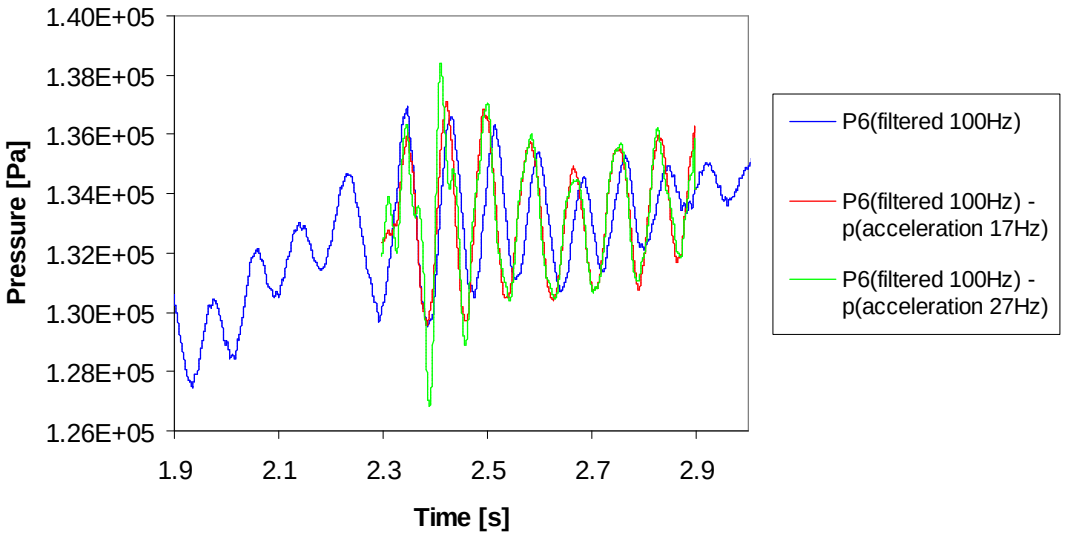

Figure 37. Filtered pool bottom pressure and pressures obtained by subtracting the effect of wall motion. Cutoff frequencies used in FFT and in filtering are shown in the legend. Time interval 2.3 … 2.9 s was used in FFT.

6.2 A simple analytical model of the pool

The pressure fluctuations caused by wall motion are studied in the following by using a simple analytical model. The pool is reduced into a single degree-of-freedom oscillator as shown in Fig. 38. In this case the pool water and the structure experience only simultaneous vertical rigid-body motion, i.e. their masses are summed to have the mass of the oscillator. Eigenmode FEM analysis of the PPOOLEX facility and also experimental results suggest that the facility undergoes predominantly vertical motion at frequency of about 10 Hz so that this simple model should not be too far from reality.

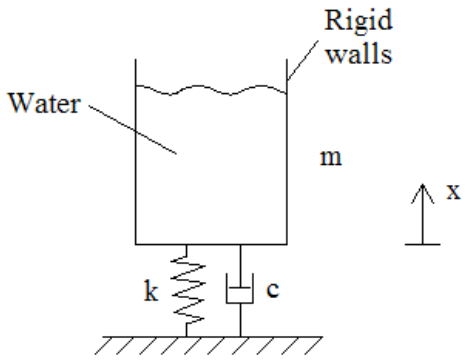

Figure 38. Simplified model of the PPOOLEX facility.

Linear second order ordinary differential equation for this system is

$$m\ddot{x} + c\dot{x} + kx = \sum_{i=1}^{N} F_i \cos(\omega_i t + \theta_i) \tag{23}$$

where m is the mass, c is the damping, k is the spring stiffness, x is the position and the upper dots stand for time-derivatives. The forcing term on the right-hand side is a sum of harmonic components each having their own amplitude, frequency and phase. The undamped and damped natural frequencies of the system are (Greenberg, 1998)

$$\omega_0 = \sqrt{\frac{k}{m}} \tag{24}$$

$$\omega_{0,d} = \sqrt{\omega_0^2 - \left(\frac{c}{2m}\right)^2} \tag{25}$$

Steady state solution caused by forcing component i is

$$x_i(t) = \frac{F_i}{Z_{m,i}\omega_i} \cos(\omega_i t + \phi_i) \tag{26}$$

where

$$Z_{m,i} = \sqrt{c^2 + \left(\omega_i m - \frac{k}{\omega_i}\right)^2} \tag{27}$$

$$\phi_i = \theta_i + \phi'_i \tag{28}$$

$$\phi'_i = \text{atan}\left(\frac{c}{\omega_i m - k/\omega_i}\right), \quad 0 \le \phi'_i \le \pi \tag{29}$$

Velocity and acceleration of the pool are then

$$\dot{x}_i(t) = -\frac{F_i}{Z_{m,i}}\sin(\omega_i t + \phi_i) \tag{30}$$

$$\ddot{x}_i(t) = -\frac{F_i \omega_i}{Z_{m,i}}\cos(\omega_i t + \phi_i) \tag{31}$$

The responses caused by different forcing components can be summed because (23) is linear. We can now study what parameters of the pool affect most on the pressure fluctuations due to wall motion, i.e. on the pool acceleration. Close to the resonance point, i.e. when $\omega_i \approx \omega_0$, we have

$$Z_{m,i} \approx c \tag{32}$$

and magnitude of the acceleration is determined by the pool damping

$$\ddot{x}_i(t) = -\frac{F_i \omega_i}{c}\cos(\omega_i t + \phi_i) \tag{33}$$

The pool damping is relatively small and affects close to the resonance point. If the damping is neglected, we have

$$Z_{m,i} = \sqrt{\left(\omega_i m - \frac{k}{\omega_i}\right)^2} = \left|\omega_i m - \frac{k}{\omega_i}\right| = \frac{\left|\omega_i^2 - \omega_0^2\right| m}{\omega_i} \tag{34}$$

and the acceleration becomes

$$\ddot{x}_i(t) = -\frac{F_i \omega_i^2}{\left|\omega_i^2 - \omega_0^2\right| m}\cos(\omega_i t + \phi_i) \tag{35}$$

Obviously close to the resonance point the acceleration becomes large and modifying either *m* or *k* has the desired effect. If we assume $\omega_i >> \omega_0$, we obtain

$$Z_{m,i} \approx \omega_i m \tag{36}$$

and

$$\ddot{x}_i(t) = -\frac{F_i}{m}\cos(\omega_i t + \phi_i) \qquad (37)$$

Eqs. (33) and (37) show that increasing damping and mass of the pool would be effective for suppressing the pressure fluctuations. This makes sense also intuitively as damping suppresses the pool motion and a heavy pool is more difficult to accelerate. In the experiments, the largest pressure fluctuations occur at the natural frequency. Therefore, increasing the pool damping would probably be most effective.

Results of the above analysis are tested in the following with values m = 16100 kg, k = 123 MN/m and c = 58 kNs/m which resemble values of the PPOOLEX facility. Undamped and damped natural frequencies of this system are f_0 = 13.93 Hz and $f_{0,d}$ = 13.92 Hz so the effect of damping is fairly small. Pressure on the pool floor is taken from a CFD calculation similar to that presented in Sec. 5.1.1, a constant velocity of 10 m/s was used at the pipe inlet. Pressure signal from the CFD calculation is presented in Fig. 39. FFT is conducted on the pressure load and the problem is solved in the frequency-space.

Fig. 40 shows frequency spectrum of the pressure load. The highest amplitudes are at 3 - 4 Hz which corresponds to formation of bubbles at the pipe outlet. The resulting displacement response of the pool is shown in Fig. 41; the response obviously has a peak close to the natural frequency of the system.

Pressure responses at the pool floor with different pool parameters are presented in Fig. 42. These plots confirm the results of the above mathematical analysis. First, the pool damping has a large effect close to the resonance point. Second, increasing the pool mass suppresses the pressure oscillations for high frequency load components. Unfortunately, increasing mass of the pool structure is more difficult than changing flexibility of the supports in the PPOOLEX facility. Increasing structural damping would probably also be difficult. The difference between the load frequency and natural frequency of the pool has to be considered also since the resonance point of the pool must obviously be avoided.

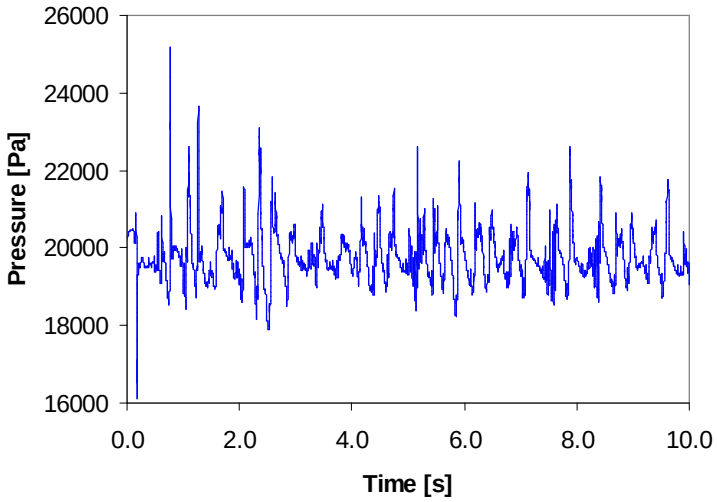

Figure 39. Average pressure on the pool floor as a function of time during blowdown of air. The pressure has been obtained with the axisymmetric CFD model presented in Sec. 5.1.1.

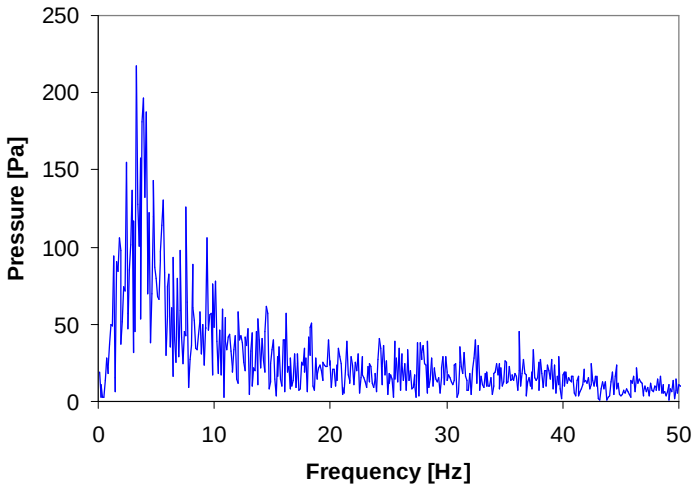

Figure 40. Frequency content of the pressure load in Fig. 39 obtained from FFT.

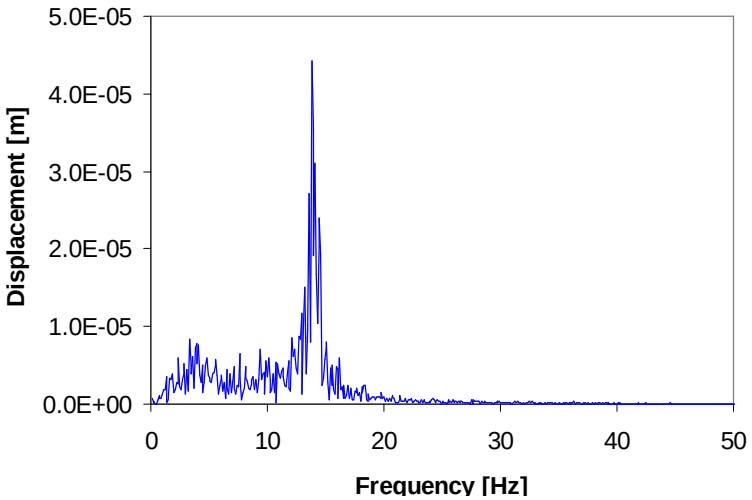

Figure 41. Displacement response of analytical model of the pool.

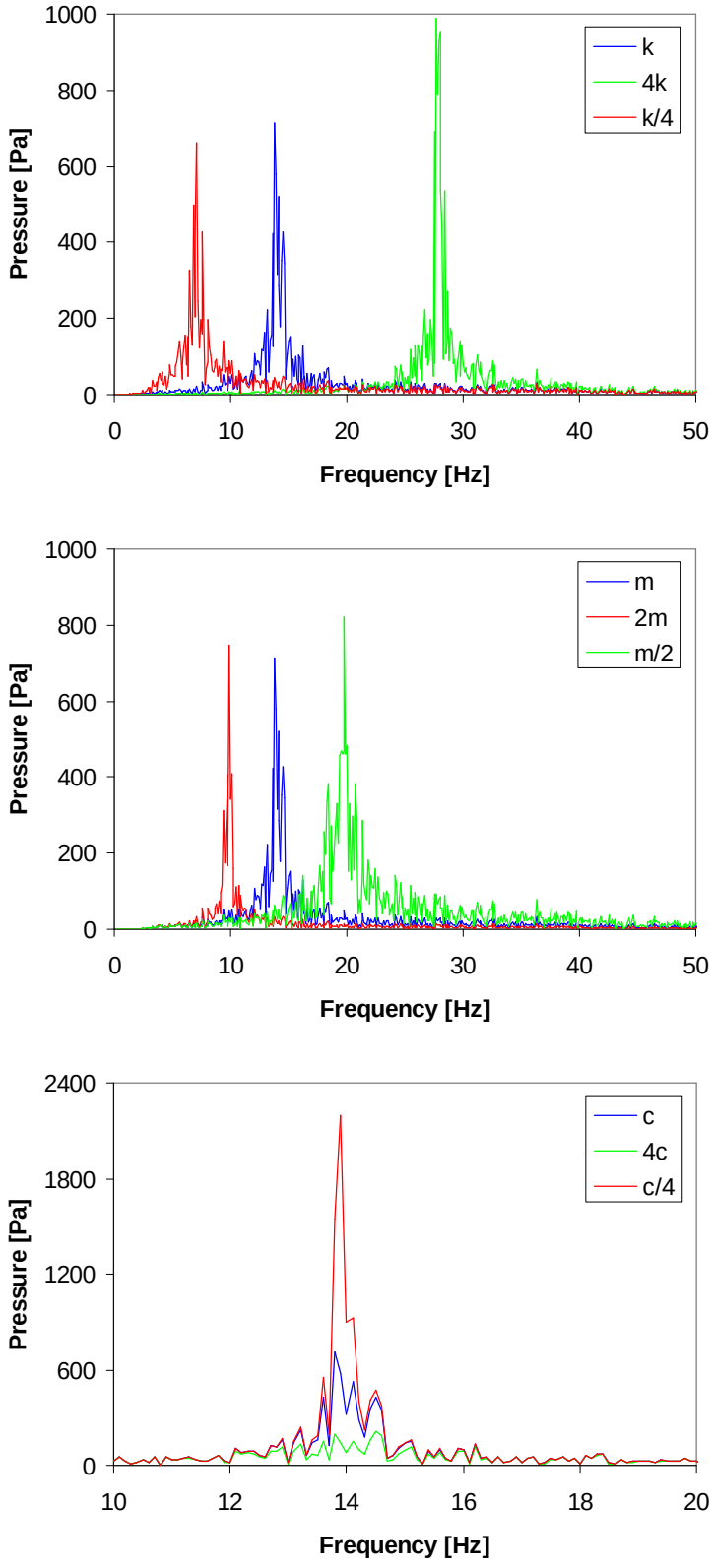

Figure 42. Effect of spring stiffness, mass and damping on the pressure fluctuations caused by wall motion in analytical model of the pool.

6.3 Calculations with axisymmetric model of the pool

The pressure load shown in Fig. 39 was applied on the axisymmetric acoustic-structural ABAQUS model (see Sec. 5.1) for studying the effect of the pool parameters in a more realistic case. Fig. 43 shows pressure signals on the pool floor; the resulting acoustic pressure has been added to the pressure with rigid walls in order to have the total pressure. Clearly the pressure load is masked by the wall motion induced pressure fluctuations after the initial phase, i.e. after the pipe clearing. Fig. 42 shows effect of the pool parameters on the pressure fluctuations. Also in this case increasing damping and mass of the pool are most effective. However, no large effects can be seen with the used values.

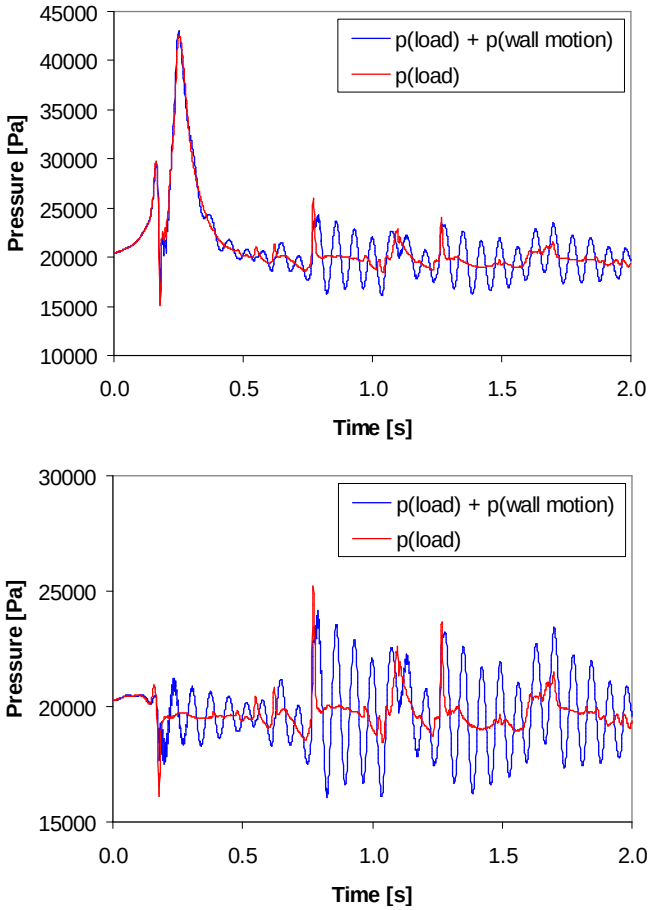

Figure 43. Total pressure and pressure due to blowdown load on pool floor in axisymmetric model. Upper: below blowdown pipe, lower: average pressure.

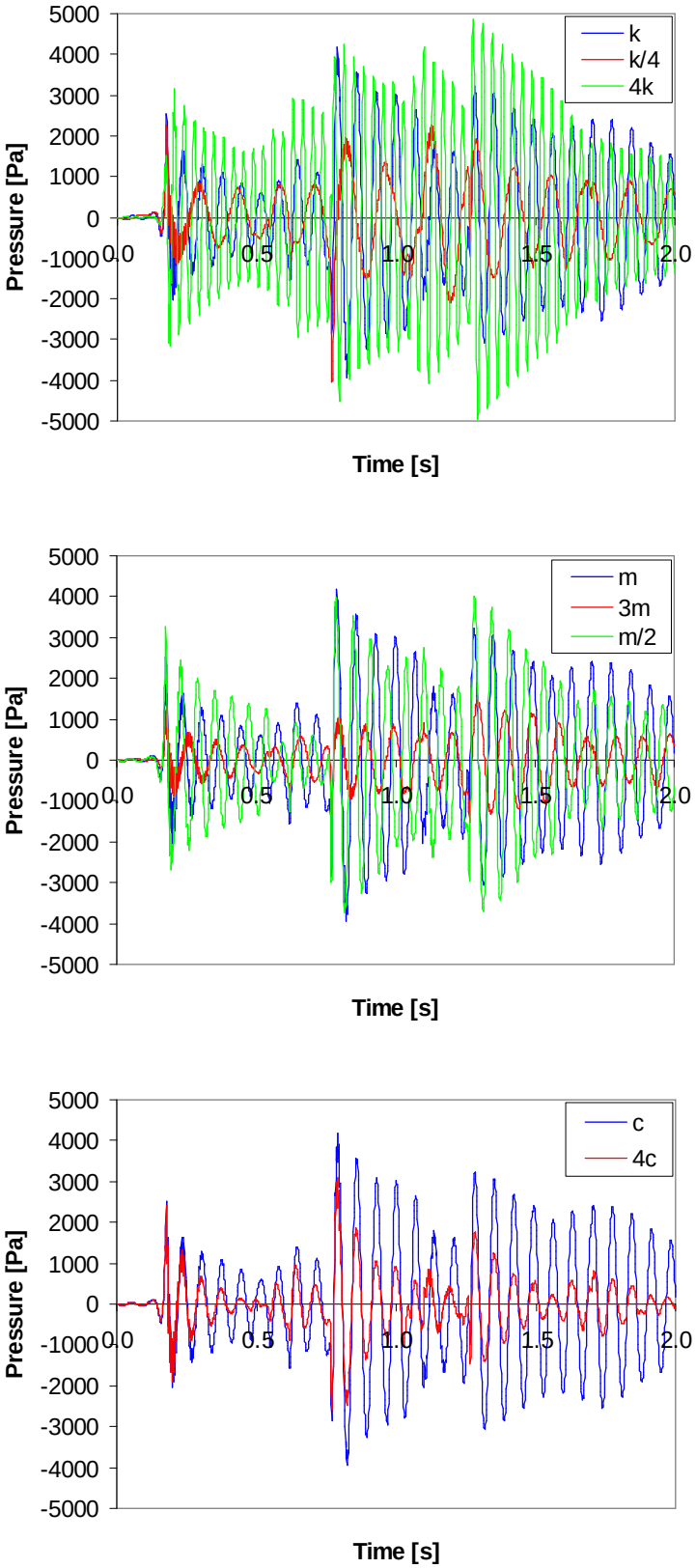

Figure 44. Effect of spring stiffness, mass and damping on the pressure fluctuations caused by wall motion in axisymmetric model. Note that in the middlemost figure "m" refers to mass of the pool structure, i.e. without water.

6.4 Suggestions for the experimental facility

An acceleration sensor at the pool bottom could be obviously used for measuring the acceleration and hence for estimating the pressure fluctuations according to Eq. (22). However, it seems that it would be possible to directly measure the pressure fluctuations e.g. with the arrangement shown in Fig. 45. There is a small-diameter steel pipe welded at the pool bottom and filled with water up to the same level as the pool water. As the water in the pipe is isolated from the pool water, it does not see the blowdown load but only the pressure fluctuations due to wall motion. This is of course if the pipe wall is sufficiently rigid, but this should not be a problem for any small-diameter steel pipe having a reasonable wall thickness.

One way is to measure pressure at points 1 and 2 in Fig. 45 with two separate sensors and then determine the blowdown pressure from Eq. (21). Another way is to measure directly the pressure difference between the two points with a single sensor. The latter might be more accurate but the former would give also the wall motion induced pressure fluctuations which could be beneficial.

Due to practical reasons it might be preferable to attach the pipe to the pool side wall as shown in Fig. 45 and hence measure the pressure from the bottom corner. This is also correct because of the potential flow assumption used in the methods that require the pressure source (Pättikangas et al., 2008).

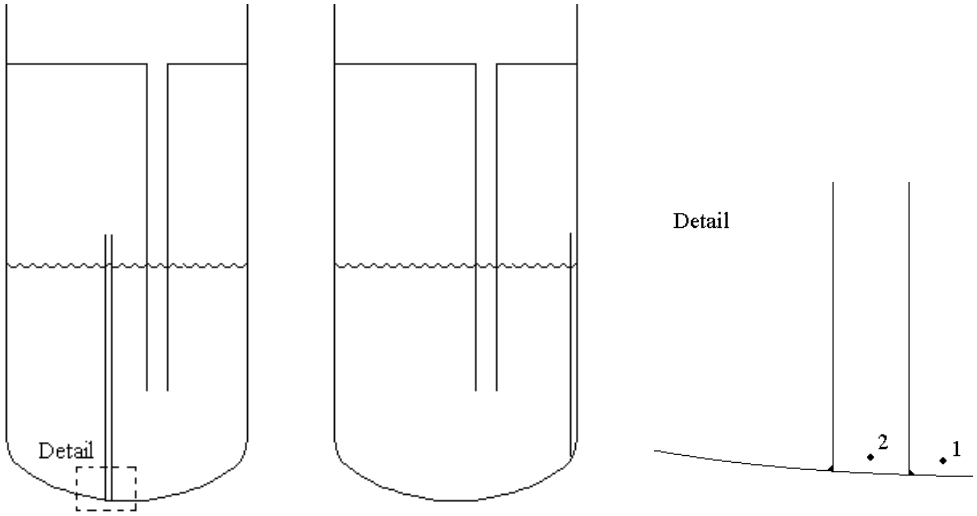

Figure 45. Schematic of small-diameter pipe inside the pool. Two possible locations for the pipe are depicted.

7 Conclusions

PPOOLEX experiment WLL-04-02 on wall condensation of vapour has been studied with CFD simulation. Wall condensation model has been adapted to an Euler-Euler multiphase model of the Fluent CFD code for this purpose. In addition, a simple direct-contact condensation model has also been included in the code. The main features of the experiment were captured by the CFD simulation.

The main focus of the CFD modelling work was on modelling condensation in the drywell. The amount of condensation found in the CFD was in fair agreement with the experiment. The comparison is, however, hampered by the delay of the condensate flow from the drywell walls via the aqueduct system to the collection tanks. Further investigations of the delay in the experiment can improve the comparison. In addition, a longer CFD simulation would improve the accuracy of the comparison.

The modelling of heat transfer between the gas and the liquid phase in the regions far away from the walls of drywell was based on the Ranz-Marshall model readily available in Fluent. According to the present calculations the bulk condensation is significant in the early phase of the discharge and the modelling of bulk condensation should be improved.

The vortex flow meter has some delay in the start of the discharge. In the present work, the measured value was used as a boundary condition of the CFD simulation without making any corrections. The delay should be taken into account in future work because it affects the results of short CFD simulations. In longer simulation, this inaccuracy is not so important.

The present simulation was so short that the gas flowing into the wetwell contained significant amount of air. The mole fraction of vapour at the outlet of the vent pipe had the maximum value of about 0.3. Therefore, the non-condensable gas strongly affected the direct-contact condensation in the water pool. Much longer simulations are needed in order to study jugging and condensation oscillations. Another alternative would be starting the CFD simulation in the middle of a discharge. Determination of the initial conditions for the simulation would then be a challenge.

FSI calculations of the experiments were performed by using the Star-CD, ABAQUS and MpCCI codes. An approximate method that makes possible numerically stable FSI calculations for the experimental facilities was used. The method is based on linear perturbation method which necessitates small structural deformations. The calculations showed that FSI has to be taken into account for the POOLEX facility which has relatively light structures. FSI has to be accounted for also in modeling the PPOOLEX experiments if the pressure fluctuations due to wall motion are to be captured; wall pressure in the experiments and FSI calculations show clearly the oscillating component caused by wall motion. FSI may have to be accounted for in condensation pool simulations because the pool water modifies eigenfrequencies of the structure. Using only one-way coupling does not necessarily yield conservative results in

this kind of situation. The linear perturbation method was validated also against moving-mesh calculations by using different blowdown velocities and amplitudes of the wall motion.

A way for determining the pressure source for the acoustic model from pressure measured at the pool bottom was examined. Separation of the pressure component due to wall motion from the blowdown load was attempted by conducting a Fourier analysis on the measured displacement signal. The study showed that in practise sufficiently accurate acceleration signal cannot be obtained this way because the transformed signal gets easily out of phase. Simple analytical and acoustic models of the pool were also used for studying the pressure fluctuations caused by wall motion. The calculations showed that structural damping of the pool would be the most significant parameter in suppressing the pressure fluctuations. In addition, a heavy pool would be favourable assuming that the resonance point is avoided. Either of these parameters is, however, difficult to modify in practise. A measurement system was proposed which could be used for determining the pressure fluctuations.

References

Björndahl, O. and Andersson, M., 1998. Globala vibrationer vid kondensationsförlopp i wetwell orsakade av LOCA i BWR-anläggningar, SKI Rapport 99:3.

Cook, R., Malkus, D., Plesha, M. and Witt, R., 2002. Concepts and applications of finite element analysis. Wiley & Sons, Inc.

Giencke, E., 1981. Pressure distribution due to a steam bubble collapse in a BWR pressure suppression pool. Nuclear Engineering and Design, 65, pp. 175-196.

Greenberg, M.D., 1998. Advanced engineering mathematics. 2nd edition. Prentice-Hall.

Huber, P.W., Kalumuck, K.M. and Sonin, A.A., 1979. Fluid-structure interactions in containment systems: small-scale experiments and their analysis via a perturbation method. 5th International Conference on Structural Mechanics in Reactor Technology, 1979.

Laine, J. and Puustinen, M., 2008. Steam line rupture experiments with the PPOOLEX test facility. Research Report CONDEX 2/2007, Lappeenranta University of Technology, Nuclear Safety Research Unit.

Laine, J. and Puustinen, M., 2009. PPOOLEX experiments on wall condensation. Research Report CONDEX 3/2008, Lappeenranta University of Technology, Nuclear Safety Research Unit.

Puustinen, M., 2008. Personal communication.

Pättikangas, T., Timperi, A., Niemi, J. and Kuutti, J., 2008. Modelling of blowdown of air in the pressurized PPOOLEX facility, VTT Technical Research Centre of Finland, Research Report VTT-R-02233-08, Espoo, Finland, 85 p.

Sonin, A.A., 1980. Rationale for a linear perturbation method for the flow field induced by fluid-structure interactions. Journal of Applied Mechanics **47** pp. 725-728.

Timperi, A., Pättikangas, T. and Niemi, J., 2007. Analysis of loads and fluid-structure interactions in a condensation pool, VTT Technical Research Centre of Finland, Research Report VTT-R-01365-07, Espoo, Finland, 41 p.

Title Modelling of blowdown of steam in the pressurized PPOOLEX facility

Author(s) Timo Pättikangas, Jarto Niemi and Antti Timperi

Affiliation(s) VTT Technical Research Centre of Finland

ISBN 978-87-7893-278-5

Date December 2009

Project NKS-R / POOL

No. of pages 52

No. of tables -

No. of illustrations 45

No. of references 11

Abstract

PPOOLEX experiment WLL-04-02 on condensation of vapour is studied with CFD simulations. Wall condensation model has been adapted to an Euler-Euler multiphase model of the Fluent CFD code for this purpose. In addition, a simple direct-contact condensation model has also been included in the code.

The main focus of the CFD modelling work was on modelling condensation in the drywell. The amount of condensation found in the CFD calculation was in fair agreement with the experiment. The present simulation was so short that the gas flowing into the wetwell contained significant amount of air. The mole fraction of vapour at the outlet of the vent pipe had the maximum value of about 0.3. Therefore, the non-condensable gas strongly affected the direct-contact condensation in the water pool. Much longer simulations are needed in order to study jugging and condensation oscillations.

FSI calculations of the experiments were performed by using the Star-CD, ABAQUS and MpCCI codes. An approximate method that makes possible numerically stable FSI calculations for the experimental facilities was used. The method is based on linear perturbation method which necessitates small structural deformations. The calculations showed that FSI has to be taken into account for the POOLEX facility which has relatively light structures.

A way for determining the pressure source for the acoustic model from pressure measured at the pool bottom was also examined. Separation of the pressure component due to wall motion from the blowdown load was attempted by conducting a Fourier analysis on the measured displacement signal. The study showed that in practise sufficiently accurate acceleration signal cannot be obtained this way because the transformed signal gets easily out of phase. A measurement system was proposed which could be used for determining the pressure fluctuations.

Key words Condenstion pool, pressure suppression pool, BWR, CFD, fluid-structure interaction, FSI